# POLYTECHNIC OF TURIN

## Department of Electronics and Telecommunications



Master's Degree in Biomedical Engineering

# Effects of Dehydration on the Inferior Vena Cava

Supervisors

Prof. Luca MESIN

Dr. Piero POLICASTRO

Candidates

Alessandra MATTANA

Umberto MACRÌ

A.Y 2023/2024

*Grazie*

# Abstract

Currently, the hydration status of human subjects is assessed through either invasive techniques, e.g. the blood sample analysis or time-consuming laboratory methods such as the analysis of urine. The hydration status plays a crucial role in athletic performance and recovery. Athletes and physically active individuals must carefully manage their fluid intake to maintain optimal performance levels and reduce the risk of dehydration, which can lead to impaired physical abilities, cognitive functioning, and even injury. The aim of this study is to assess, with ultrasound, whether the diameter and the pulsatility of the inferior venca cava (IVC) can use as indicators of the hydration status. The pulsatility is expressed by the caval index (CI), which is the variation of the diameter in relation to the maximum one. The parameters were extracted with VIPER s.r.l. software using longitudinal section ultrasound videos of IVC. The software automatically tracks the IVC, allowing for parameter extraction from each frame. An experimental protocol was designed to induce dehydration in the participants through physical activity by 10-minute walk repeated for five times. Ultrasound images and weight were taken at the beginning of the protocol and after each trial, approximately in 3 minutes. Finally, participants were rehydrated, and the hydration status was assessed through ecographic imaging conducted at 2, 4, and 6 minutes later. The sample consisted of 37 healthy subjects (18 females and 19 males), aged $24.24 \pm 1.92$ years. The results show a significant decrease in the diameter ($\Delta D$) after 50 minutes of activity in comparison to the initial diameter ($\Delta D = 2.02$ mm, $p$-value $< 0.02$) and a significant increase during the rehydration phase ($\Delta D = 1.86$ mm, $p$-value $< 0.03$). No notable differences were identified in the caval index between the baseline and the 50-minute post-activity measurement ($p$-value $= 0.93$). Furthermore to verify whether the results were not the consequence of possible acquisition errors by the operator, an evaluation of both inter-operator repeatability and software was performed, resulting in a standard deviation $= 0.94$ mm and an ICC (Intraclass Correlation Coefficient) $>$ 0.9.

# Table of Contents

# List of Figures

# List of Tables

# List of Acronyms

**ADH** Antidiuretic Hormone

**BIA** Bioelectrical Impedance Analysis

**BUN** Bun Urea Nitrogen

**CCI** Cardiac Caval Index

**CI** Caval Index

**ECG** Electrocardiography

**HR** Heart Rate

**ICC** Intraclass Correlation Coefficient

**IVC** Inferior Vena Cava

**k-NN** k-Nearest Neighbors

**MAD** Median Absolute Deviation

**MS$_\mathbf{B}$** Mean Square between Subjects

**MSE** Mean Square Error

**MS$_\mathbf{W}$** Mean Square within Subjects

**PZT** Lead Zirconate Titanate

**$R^2$** Regression Coefficient

**RCI** Respiratory Caval Index

**SSE** Sum of Square Error

**SST** Sum of Square Total

**STD** Standard Deviation

**TBW** Total Body Water

**TGC** Time Gain Compensation

**US** UltraSound

# Chapter 1

# Principles of Anatomy and Physiology

## 1.1 Anatomy and physiology of the cardiovascular system

The cardiovascular system consists of three components: the blood, the heart and the blood vessels (Figure 1.1). They are responsible for transporting gases such as oxygen and carbon dioxide, nutrients like lipids, proteins and sugars, waste substances resulting from metabolism and hormones that convey chemical messages throughout the body [1]. The heart is the central element of the system, responsible of blood's propulsion, from which major blood vessels like the aorta and pulmonary arteries originate, and into which veins such as the vena cava and pulmonary veins converge. The blood vessels form a closed circuit network, distinguishing two types of circulation [1]:

- the systemic circulation: through the arteries, oxygen-rich blood is transported from the heart to the periphery of the body, where gas exchange and the exchange of substances essential for tissue sustenance occur. Finally, through the veins, oxygen-poor blood returns to the heart;

- pulmonary circulation: through the pulmonary arteries, oxygen-poor blood reaches the lungs where gas exchange takes place. Subsequently, oxygenated blood returns to the heart through the pulmonary veins (Figure 1.2).
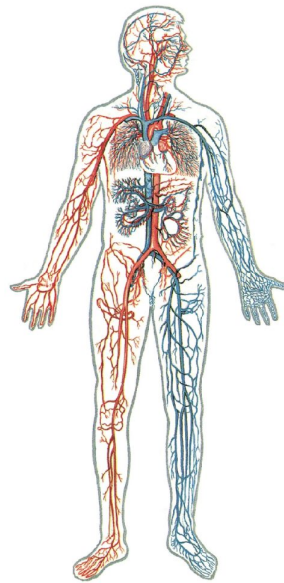
**Figure 1.1:** *Schematic representation of the vascular network: the arteries (in red) are represent on the left and the veins (in blue) on the right.*
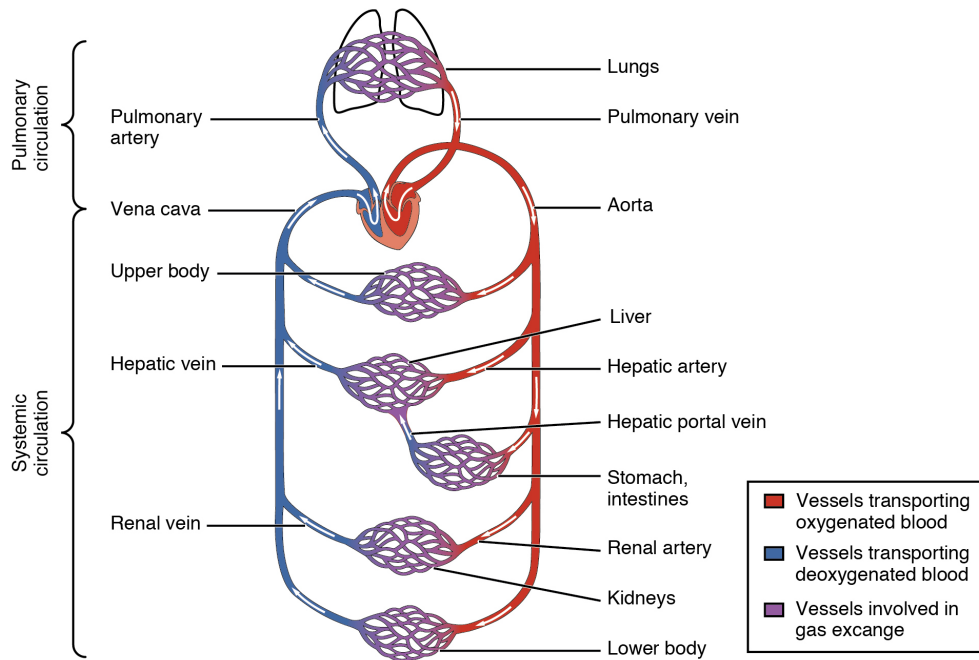


**Figure 1.2:** *Schematic representation of systemic and pulmonary circulation.*

### 1.1.1   Heart

The heart is the muscle responsible for generating the pressure difference that allows blood circulation within the vessels. The organ is composed of four chambers: two atria and two ventricles (Figure 1.3). The right atrium receives oxygen-poor blood, which flows into the right ventricle through the tricuspid valve and is subsequently pumped into the pulmonary arteries through the pulmonary valves. Oxygenated blood returns to the left atrium through the pulmonary veins, descends into the left ventricle through the mitral valve and is directed into the aorta through the aortic valve. The cardiac muscle, called myocardium, is composed by 70% muscle fibers (both striated and smooth) and 30% connective tissue [1]. This fiber composition ensures a rapid and powerful contraction (provided by the striated fibers), simultaneously over a large volume of cardiac tissue (facilitated by the smooth fibers). The heart is located in the middle mediastinum, in retro-sternal position, with its apex pointing on the left [1].
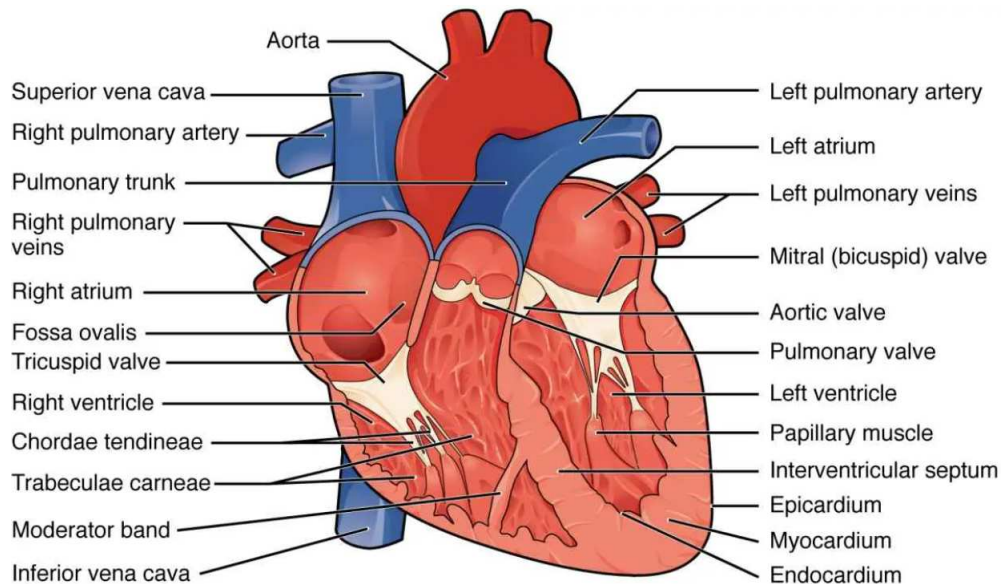
**Figure 1.3:** *Representation of the heart and its parts.*

Cardiac contraction is involuntary and regulated by the autonomic nervous system; the action potential originates from the sinoatrial node (Figure 1.4), depolarizes both atria, and subsequently reaches the ventricles through the atrioventricular node and the His bundle. Specifically, depolarization of the ventricular walls occurs almost simultaneously thanks to the Purkinje fibers that transmit the signal from the atrioventricular node throughout the volume of the ventricle, very rapidly (approximately 30 ms) [1].
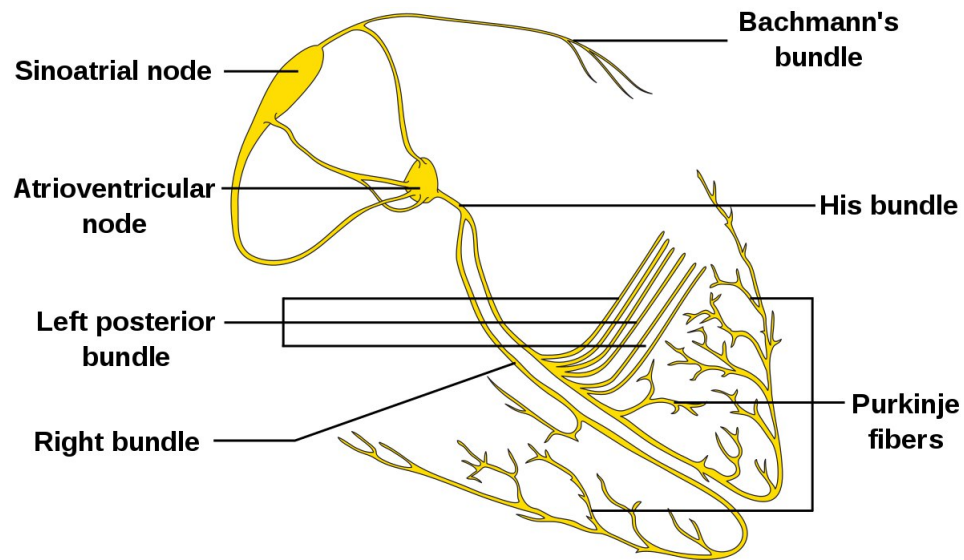
**Figure 1.4:** *Representation of pacemaker cells and their distribution within the heart.*

## 1.1.2 ECG waveform

The electrical activity of the heart is recorded through electrodes placed on the skin, near the heart. The signal obtained is the electrocardiogram (ECG) formed by positive and negative deflections connected by isoelectric segments. The sequence of deflections repeats approximately the same for each cardiac cycle, with a frequency depending on the heart rate. Considering the first derivation (from the right to the left hand in Einthoven triangle [2]) of a complete electrocardiogram, that can be observed in Figure 1.5 [1]:

- P wave: corresponds to atrial depolarization, it has a reduced amplitude because atrial depolarization is not powerful;

- PQ interval: isoelectric line describing the atrioventricular conduction time;

- Q wave: a small negative amplitude, it corresponds to the depolarization of the interventricular septum;

- R wave: corresponds to the depolarization of the apex of the left ventricle;

- S wave: corresponds to the depolarization of the posterior region of the left ventricle;

- ST interval: isoelectric segment representing the period of time when the entire ventricle is depolarized;

4

- T wave: represents ventricular repolarization;

- U wave: not always visible, it represents the depolarization of the papillary muscles present inside the ventricular cavities.

The repolarization of the atrial chambers is not visible in the first derivation of ECG trace as they are covered by the QRS complex.

The amplitude of the ECG signal varies from 0.5 to 4 mV, and the bandwidth is between 0.01 and 250 Hz [2]. From the analysis of the signal, some parameters can be extracted, including heart rate, heart rate variability, and the presence of cardiac pathologies.
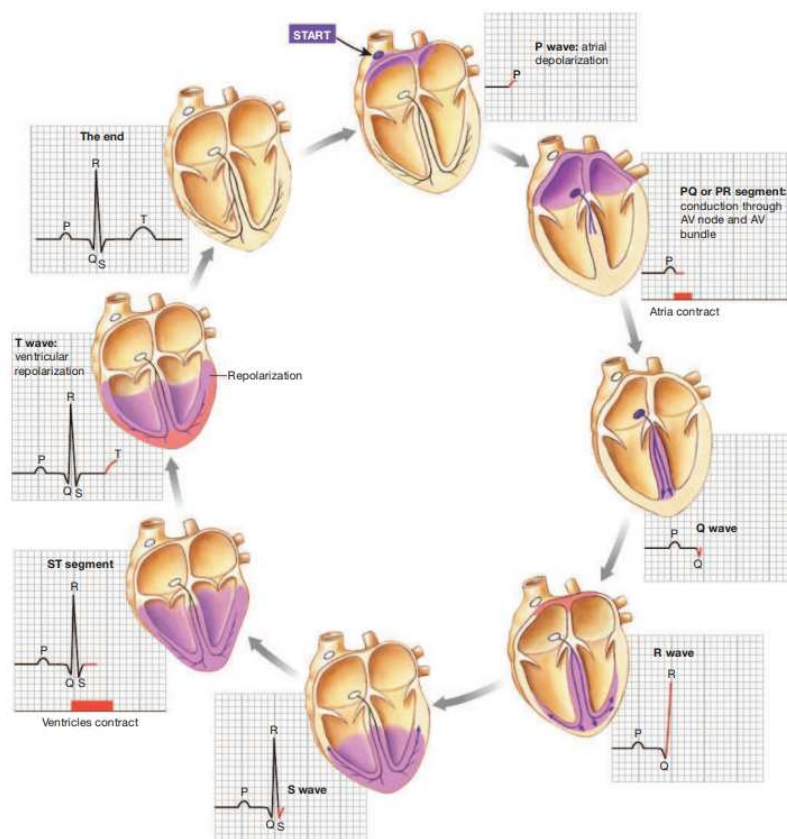


**Figure 1.5:** *ECG waveform compare to cardiac cycle.*

### 1.1.3 Arteries and veins

Veins and arteries are the vessels through which blood flows, originating in the heart and traversing the entire body. Both veins and arteries are composed of

three layers: the intima consisting of endothelial cells, the media composed of smooth muscle tissue, and the adventitia consisting of highly elastic connective tissue. Arteries have a thicker muscular tissue, double that of veins, despite both having a comparable external diameter (between 4 mm and 5 mm) [1]. Another difference consists in the presence of one-way, swallowtail-shaped valves for the veins outside the thoracic cavity: these valves ensure that blood flow is directed from the periphery to the heart, preventing backflow and stagnation along the vein lumen (Figure 1.6) [1].

Arteries behave like pressure reservoirs, accumulating elastic energy during cardiac contraction (systole) and releasing it when the effect of the cardiac pump is absent (diastole); blood flow is guaranteed by the cardiac pump during ventricular systole, while during diastole, the passive restriction of the thick muscular and elastic tissue allows the transfer of accumulated energy to the blood. This behavior ensures an almost laminar blood flow in the body, avoiding a pulsatile pattern that would hinder substance exchange at the capillary level (Figure 1.7).

Veins, on the other hand, have thinner and more easily stretchable walls compared to arteries of the same size, allowing for the passage of a large volume of blood without significant resistance from the walls. They can be considered volume reservoirs as they easily respond to changes in blood volume and can contain 60% of the total blood volume (Figure 1.8) [1].
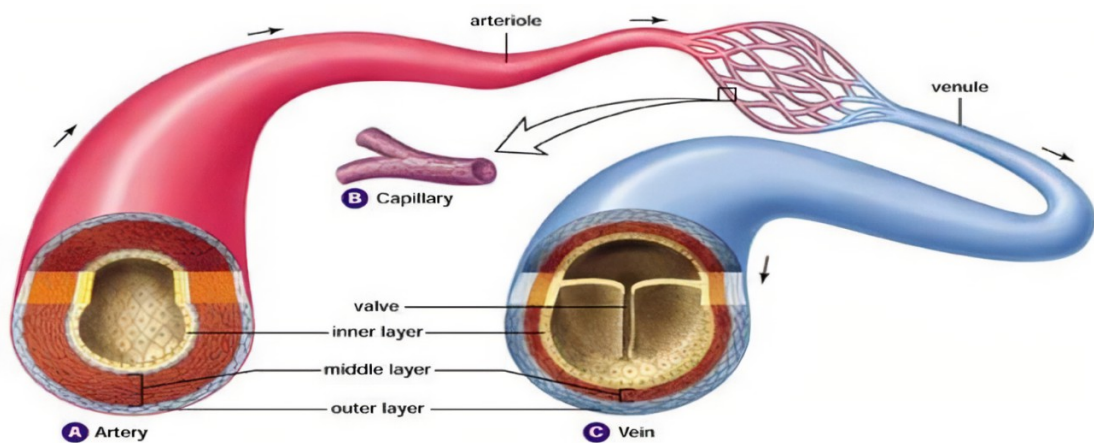


**Figure 1.6:** *Anatomical differences between arteries and veins.*
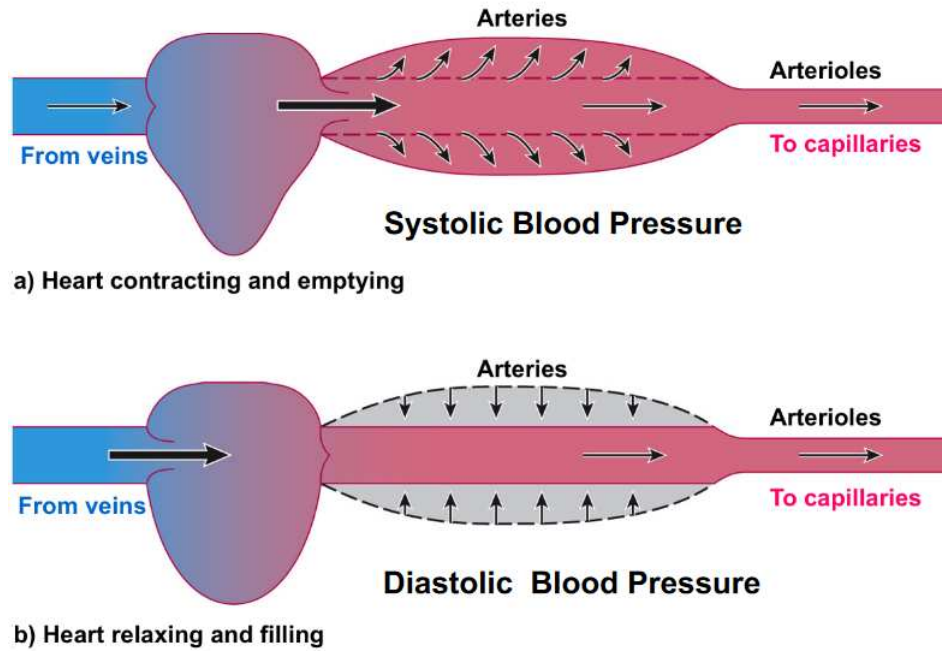
**Figure 1.7:** *Arteries behavior as a pressure reservoirs. a) Heart emptying phase correspond to a dilation of the arteries, b) Heart filling phase correspond to a constriction of the artieres.*
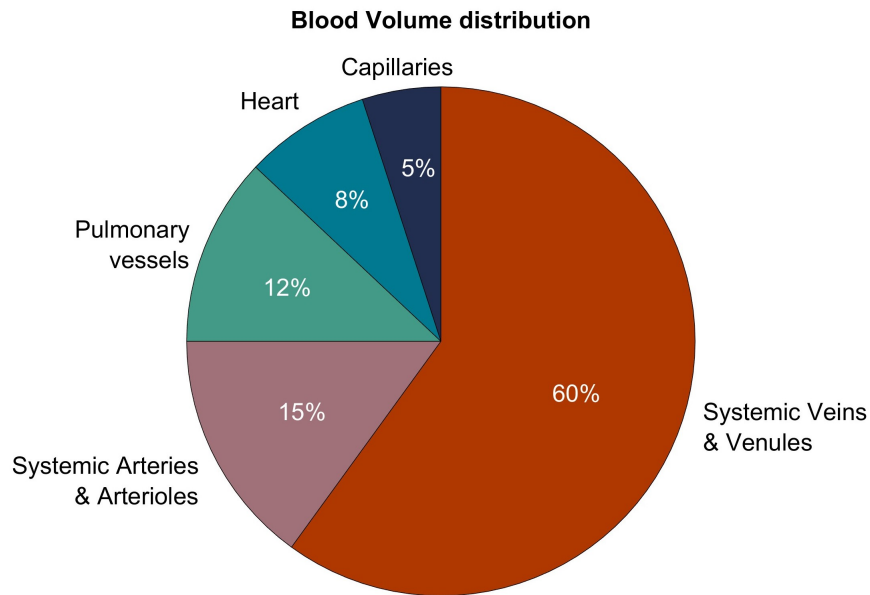


**Figure 1.8:** *Volume distribution of blood in circulatory system. 60% is found within the veins.*

### 1.1.4 Vascular compliance and effects of blood pressure on IVC

Vascular compliance is the physiological capacity of a vessel to change its lumen size in response to changes in transmural pressure, which is defined as the difference between the internal and external pressure on a blood vessel. Total compliance ($C_{tot}$) depends both on the type of tissue which composes the vessel (vascular compliance $C_v$) and the elasticity of the surrounding tissues (extra-vascular compliance $C_{ev}$): when the external tissues are very rigid, they do not allow the vessel to expand; therefore, the total compliance value is always less than the vascular compliance. The total compliance is calculated as [3]:

$$C_{tot} = \frac{C_{ev} \cdot C_v}{C_{ev} + C_v} \tag{1.1}$$

At the same pressure, vessels with greater compliance deform more easily compared to those with lower values: veins have a compliance value 30 times greater than arteries [1]. Since the internal pressure ($\Delta P$) of the vessel is not always constant, the volume ($\Delta V$) of the vessels also varies proportionally to the compliance according to the law:

$$C_{tot} = \frac{\triangle V}{\triangle P} \tag{1.2}$$

where the volume is measured in ml and the pressure in mmHg. The volume-pressure curve (Figure 1.9) shows that, with the same pressure change, there is a greater volume variation at lower pressures [3].
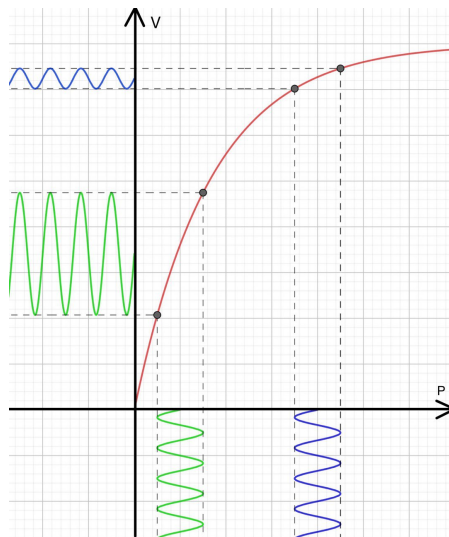


**Figure 1.9:** *Curve volume-pressure.*

An increase in systemic pressure leads to a greater inflow of blood into the IVC and a consequent dilation of the vessel: in veins, the pressure is lower than in arteries, and a change in pressure will result in a greater change in volume. This is why the inferior vena cava is distinguishable from other arterial vessels in images.

### 1.1.5 Inferior vena cava

The inferior vena cava transports blood from the sub-diaphragmatic regions to the heart, carrying 80% of the venous return [1]. It originates in the abdominal cavity at the level of the L5 vertebra, from the union of the two iliac veins, and empties into the right atrium of the heart [1]. Its course runs along the right side of the vertebral column, and during its ascending phase, it encounters other venous districts (Figure 1.10) such as the hepatic veins, adrenal veins, renal veins, lumbar veins, and superior phrenic veins, which converge into the main venous trunk of the IVC.
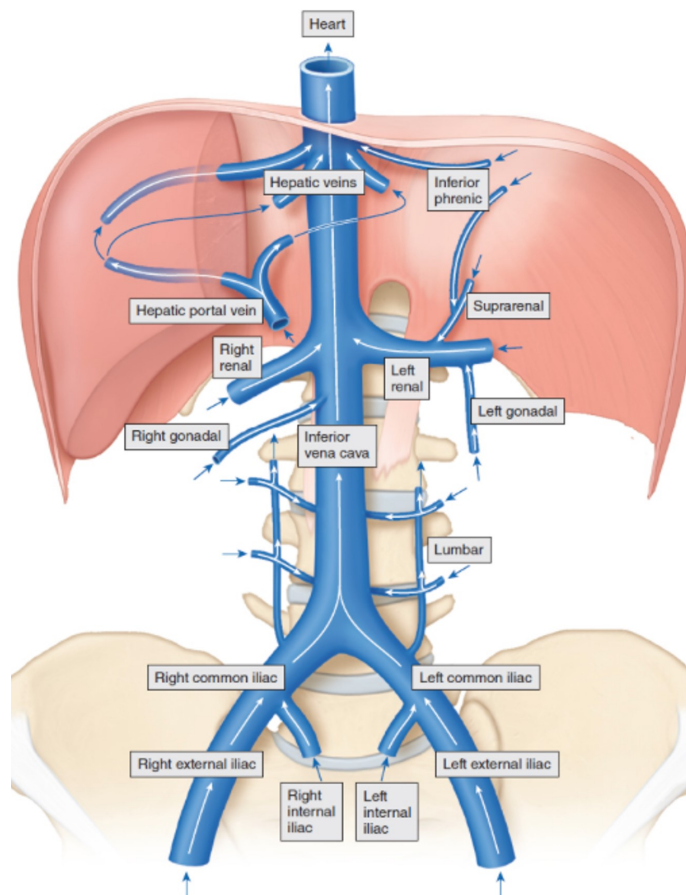
**Figure 1.10:** *Anatomy of the vena cava and confluent structures.*

It is approximately 22 cm long with a variable diameter depending on the portion of the vein considered: at its origin, it has a diameter of 20 mm, at the terminal part, it reaches a diameter of 33 mm, in the diaphragmatic portion it is 27 mm wide andin the portion of the hepatic veins ranges from 15 mm to 25 mm. [1]. The inferior vena cava is the largest vein in the human body and has a propulsive structure with a single small semilunar valve called the valve of Eustachius located in the terminal portion [1].

To assess the pulsatility of the inferior vena cava, the caval index is used, calculated as follows:

$$CI = \frac{max(D) - min(D)}{max(D)} \tag{1.3}$$

where D represents the diameter value at a specific section of the inferior vena cava. Values of the caval index close to 0 represent low pulsatility, while values near 1 indicate high pulsatility of the vein.

The peak value in the diameter trend of the inferior vena cava (IVC), known as the A wave [4], corresponds to the maximum filling of the IVC, which occurs simultaneously with the maximal emptying of the right atrium. At this moment, the tricuspid valve remains closed, preventing the backflow of blood and allowing the vein to retain its peak volume.

### 1.1.6 Maximum heart rate and definition of aerobic thresholds

The maximum heart rate that an individual can achieve is fuction of several factors, including age, gender and level of physical conditions [1]. A simple technique for estimating maximum heart rate is proposed in [5] and is given by the Cooper formula:

$$HR_{max} = 220 - Age \tag{1.4}$$

Additional techniques for more precise estimation of the maximum frequency are those based on graded exercise test (GXT) [6].

The estimation of maximum heart rate can prove useful in the assessment of an activity's intensity, enabling a comparison to be made between the subject's heart rate and the maximum heart rate:

$$HR_{\%} = \frac{HR}{HR_{max}} * 100 \tag{1.5}$$

alternatively, the intensity of exercise can be measured by the volume of oxygen consumed per minute (VO2) [6].

The percentage calculated in 1.5 can be utilized to approximate the subject's metabolic state. If the heart rate percentage is greater than 60%, the subject is in

an aerobic exercise state until reaching 90%, where they tend to be in an anaerobic state [7].

## 1.2 Anatomy and physiology of the respiratory system

The respiratory system is a complex of specialised organs and tissues (Figure 1.11) that facilitate the exchange of gases between the body and the external environment. Its primary function is to supply oxygen, which is essential for cellular metabolic activities, and to remove carbon dioxide, a waste product of metabolism. It consists of various structures divided into two main components: the upper respiratory tract composed of the nose, nasal cavity, mouth, pharynx, nasopharynx, larynx, and the lower respiratory tract consisting of the trachea, bronchi, bronchioles, alveoli, lungs, and respiratory muscles (diaphragm and intercostal muscles) [1]. In addition to respiration, the respiratory system has other important functions, such as regulating blood pH, dissipating body heat and moisture, increasing venous return, enabling phonation, and serving as the first barrier against external pathogens present in the air [1].

11
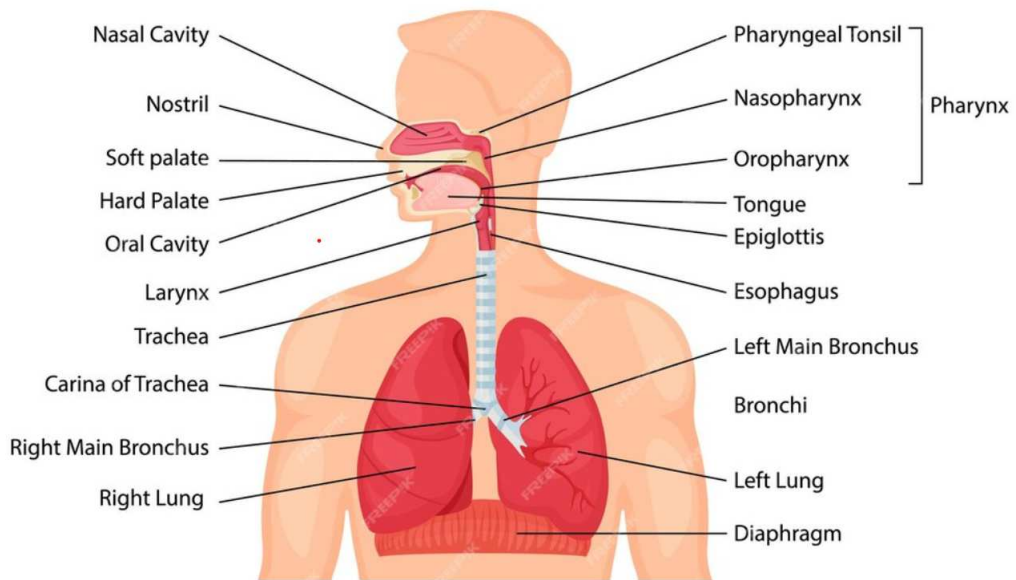
**Figure 1.11:** *Representation of respiratory system and its parts.*

## 1.2.1 Lungs and bronchi

The lungs are the main organs of the respiratory system, located within the thoracic cavity and divided into portions called lobes. They are made up of spongy and elastic tissue that allows the organ to expand during inspiration and return to its original size during the expiration phase. The right lung and the left lung differ from each other: the right lung is larger and weighs 600 grams, with three lobes (upper, middle, and lower lobes), while the left lung weighs 500 grams and is divided into only two lobes, upper and lower [1]; this size difference provides the necessary space for containing the heart. Both lungs are individually enveloped by the pleural membrane, which separates them from the thoracic cage [1]. The membrane contains pleural fluid that allows proper expansion of the organ during respiratory exchanges. Inside the pleural membrane, the pressure value is approximately -3.7 mmHg respect to external one, allowing the lung to expand along with the expansion of the thoracic cage without collapsing on itself [1].

The airflow is directed within the lungs through the trachea and the bronchial tree. The bronchial tree, as shown in Figure 1.12 is composed of [1]:

- main bronchi (one for the right lung and one for the left);

- lobar or secondary bronchi;

- segmental or tertiary bronchi;

- subsegmental bronchi;

- intralobular bronchioles;

- terminal bronchioles.
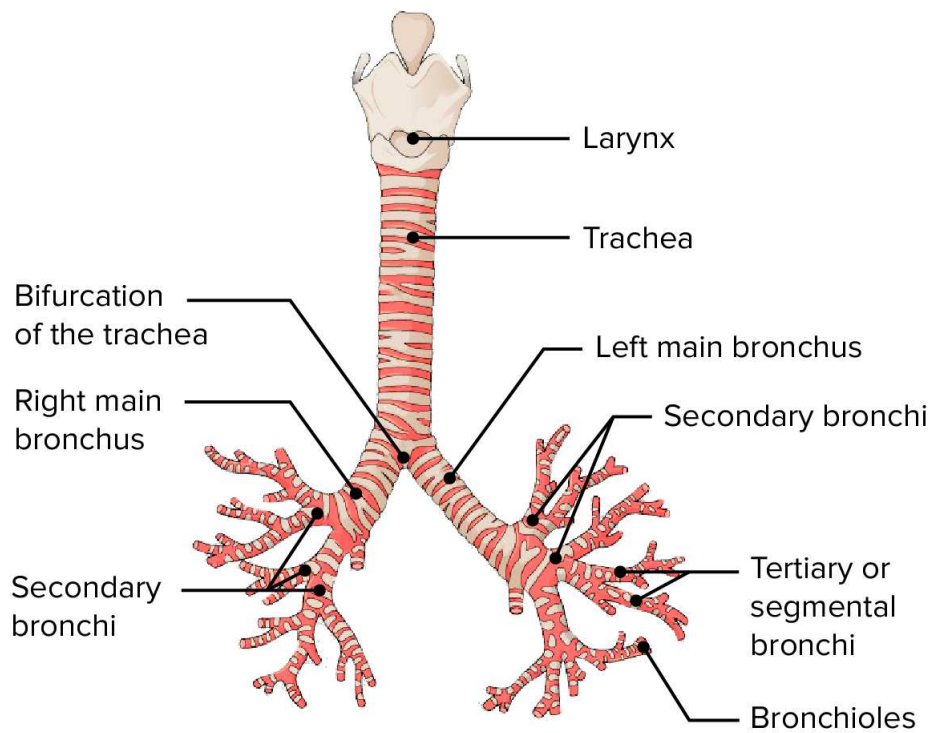


**Figure 1.12:** *Division of bronchial tree.*

In the intrapulmonary part, at the level of the bronchi, collateral branches originate (monopodial division), while at the level of the bronchioles, each branch is divided into two sub-branches of smaller diameter (dichotomous division). At the end of the bronchioles, there are alveolar ducts that terminate in the alveoli, air chambers responsible for the exchange of gases between the atmosphere and the bloodstream.

### 1.2.2  Muscles of respiration

The muscles responsible for respiratory movements are divided into two classes shown in Figure 1.13: inspiratory muscles that expand the chest cage and expiratory muscles that contract it. The diaphragm is the primary respiratory muscle, it is dome-shaped and striated, separating the chest from the abdomen [1]. During the inspiratory phase, it contracts, allowing the expansion of the lungs connected to it via the pleura and in this phase the activity of the diaphragm is assisted by the contraction of the external intercostal muscles, which cause a rotation of the ribs upwards, enlarging the chest cage. During the expiratory phase, the diaphragm relaxes, and the internal intercostal muscles contract, bringing the ribs closer together to decrease the volume of the chest cage. Additionally, there are accessory muscles that aid respiration, such as the trapezius, sternocleidomastoid, and abdominal muscles. Inspiration is a necessary movement, and the activity of all involved muscles is essential to introduce air into the thoracic cavity; conversely, expiration can also be solely passive, and air can exit due to the elastic recoil of structures, without the involvement of other muscles [1]. Respiratory muscles are responsible for generating a relative negative pressure inside the thoracic cavity, allowing air to enter the lungs according to a pressure gradient.
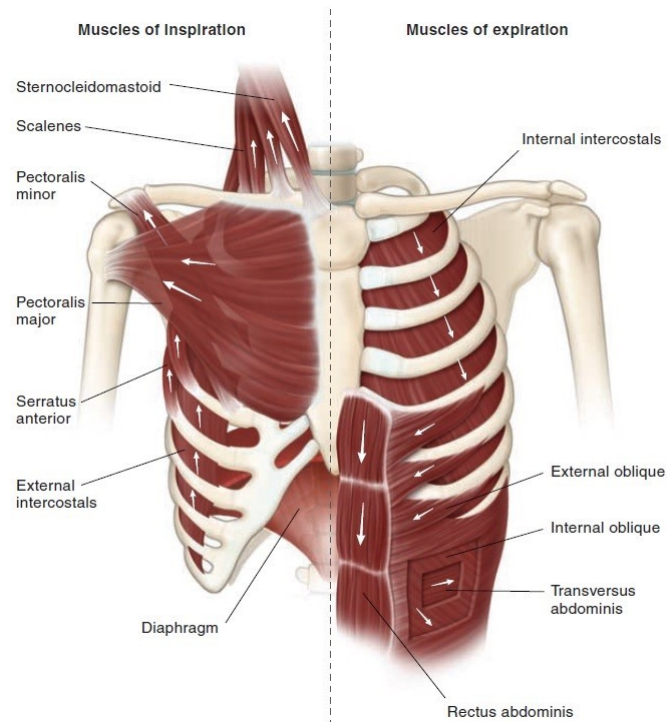


**Figure 1.13:** *Respiratory Muscles. On the left muscle of inspiration and on the right muscle of expiration.*

14

### 1.2.3  Volume, pressure and pulmonary compliance

In physiological conditions, the lungs contain approximately three liters of air, and this volume changes during the respiratory cycle: it increases during inspiration and decreases during expiration. During a normal breath, the volume of air exchanged with the external environment is approximately half a liter and it is referred to as tidal volume. Total lung capacity, which is the maximum volume the lungs can contain at the end of a maximal inspiration, is about 6 liters, conversely, residual volume, which is the volume remaining at the end of a maximal expiration, is approximately 0.5 liters [1].

The lung's internal pressure, under static conditions, equals the external pressure; nevertheless, the lung maintains a certain volume due to the intra-pleural pressure, which stands at -5 cmH2O [1]. During inspiration, air enters the lungs driven by a pressure gradient: inspiratory muscles expand the thoracic cage, causing the intra-pleural pressure to become more negative. This expansion increases lung volume, subsequently decreasing internal pressure relative to the external, allowing air to enter. Thus, what matters is the transpulmonary pressure, the difference between internal lung pressure and external pressure (pleural fluid pressure). As noted in the Figure 1.14, alveolar pressure, which is the pressure within the lungs under static conditions, is approximated to 0 cmH20 with reference to the external environment, while pleural fluid pressure is approximately -5 cmH2O. During inspiration, both pressures become more negative, causing lung volume to increase. Conversely, during expiration, pressures increase and lung volume decreases [1]. The pulmonary compliance is defined as the ratio between the change in lung volume and the change in transpulmonary pressure, providing an indication of lung elasticity [8]. Pulmonary compliance is influenced by various factors, including the elasticity of lung tissue and the surface tension at the air-fluid interface in the alveoli [1]. These factors affect how easily the lungs expand when pressure is applied. Examining the Figure 1.15, it is observed an initial phase of rapid lung expansion with a small variation in pressure, followed by a linear phase where the compliance value is calculated: expansion becomes less efficient and requires a greater variation in pressure, as the lungs encounter increased resistance to their own stretching [1]. In the final stretch, there are small volume variations after large pressure variations because the lung is nearly fully distended. In physiological conditions, lung compliance allows the lungs to expand during inspiration and contract during expiration, thus enabling gas exchange during respiration.
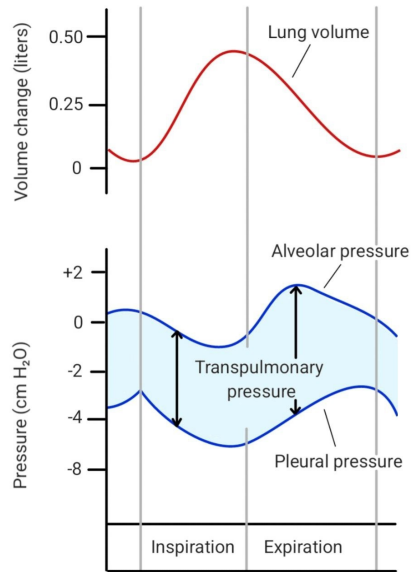
**Figure 1.14:** *Changes in lung volume, alveolar pressure, pleural pressure and transpulmonary pressure in physiological breathing.*
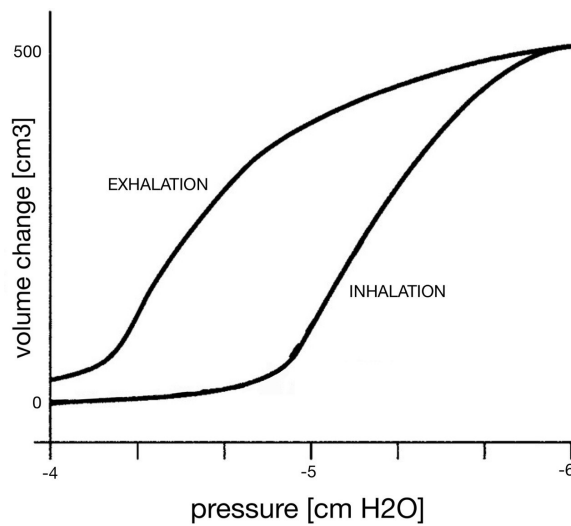


**Figure 1.15:** *Pulmonary compliance: inhalation and exhalation phases are highlighted.*

## 1.2.4  Gas exchange

Gas exchange between air and capillaries occurs within the alveoli: they pass freely through the phospholipid membranes of the cells in a process of diffusion. Bringing a gas close to a liquid results in a diffusion process until reaching concentration equilibrium; the concentration of the gas in solution is determined by Henry's law, which states that [1]:

$$C = k \cdot P \qquad (1.6)$$

where:

- C is the concentration of the gas in solution;

- P is the partial pressure of the gas in the air;

- k is the solubility of the gas.

It is noted that the amount of dissolved gas at equilibrium depends solely on the partial pressure of the gas in the air. The composition and partial pressure of gases in inspired air (Table 1.1) are different from those present in the alveoli (Table 1.2), as alveolar air is saturated with water vapor since they are lined with a thin liquid film. Also, expired air (Table 1.3) differs from alveolar air as it mixes with air from the dead space: out of 500 ml of inspired air, only 350 ml reach the lungs, the remaining portion stays in the dead space [1].

The partial pressure of oxygen in the blood is measured in mmHg and corresponds to the partial pressure of oxygen in the air required to balance the concentration of oxygen in the blood. Oxygen exchange occurs due to the difference in partial pressure gradient: venous blood has a partial pressure of oxygen of about 40 mmHg, while in the alveolar air, the value is 100 mmHg [1]. Therefore, oxygen diffuses from the gaseous environment (alveolus) to the liquid one (blood) as long as there is a partial pressure gradient. Carbon dioxide diffuses in the opposite direction due to a small gradient: the partial pressure present in the capillaries is 46 mmHg, while in the alveolus, it is 40 mmHg [1]. At the end of gas exchange, arterial blood will therefore have a partial pressure of oxygen of 100 mmHg and carbon dioxide of 40 mmHg [1]. The partial pressures of $O_2$ and $CO_2$ do not vary in the alveolar air because respiration, under physiological conditions, is a continuous process and the flow of air is constant.

**Table 1.1:** *Composition of gases and partial pressure in inspired air.*

| Gas | Inspired air composition [%] | Inspired air pressure [mmHg] |
|---|---|---|
| $O_2$ | 20.9 | 158 |
| $CO_2$ | 0.04 | 0.3 |
| $H_2O$ | 0.5 | 5.7 |
| $N_2$ | 78.6 | 596.0 |

**Table 1.2:** *Composition of gases and partial pressure in alveolar air.*

| Gas | Alveolar air composition [%] | Alveolar air pressure [mmHg] |
|---|---|---|
| $O_2$ | 13.7% | 100 |
| $CO_2$ | 5.3% | 40 |
| $H_2O$ | 6.2% | 47 |
| $N_2$ | 74.9% | 573 |

**Table 1.3:** *Composition of gases and partial pressure in expired air.*

| Gas | Expired air composition [%] | Expired air pressure [mmHg] |
|---|---|---|
| $O_2$ | 16% | 116 |
| $CO_2$ | 4.2% | 32 |
| $H_2O$ | 1.2% | 47 |
| $N_2$ | 78.6% | 565 |

## 1.2.5 Effects of respiration on IVC

The dimensions of the inferior vena cava are influenced by the pressure present in the chest and abdomen: particularly at the end of the expiratory phase, the vena cava has the largest size. During inspiration, the vena cava undergoes compression due to the decrease in intrathoracic pressure, which drains blood from the IVC. Two types of inspiration can be identified, each with slightly different effects on the IVC [3]:

1. thoracic inspiration: primarily involves the lifting of the thoracic cage, utilizing the external intercostal muscles to expand the chest cavity. In this type of inspiration, there is a slight reduction in the size of the vena cava;

2. diaphragmatic or abdominal inspiration: primarily involves the movement of the diaphragm, which descends, pulling the lungs downward. This type of inspiration occurs in relaxed conditions and reduces the involvement of accessory respiratory muscles. In this type of inspiration, there is a significant reduction in the size of the vena cava.

This has been experimentally demonstrated by various studies found in the literature, both during spontaneous respiration [9] and controlled isovolumetric respiratory efforts [10].
On the contrary, in positive pressure ventilation, the intrathoracic pressure elevation inhibits venous return, leading to augmented abdominal venous blood pressure and expansion of the inferior vena cava during inspiration (Figure 1.16).
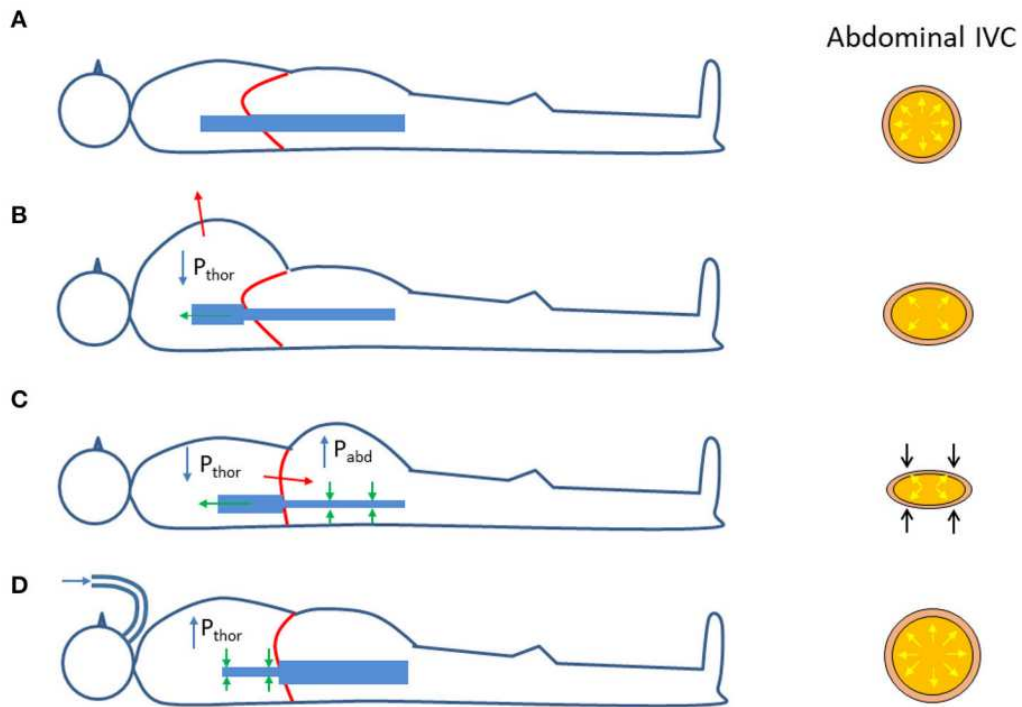
**Figure 1.16:** *Effect of respiration on the shape of the IVC. A) End espiration, B) Thoracic inspiration, C) Abdominal inspiration, D) Inspiration by ventilation.*

## 1.3 Anatomy and physiology of the sweat principle

Water constitutes approximately 50-60% of the body weight of an adult subject, with 65% of the total water being contained within cells and 35% in the extracellular part [11]. Water plays several fundamental roles in the body, including:

- maintaining the solubility of products essential for metabolic function and its waste, facilitating the transport of such products within the body [12];

- maintaining the correct blood volume;

- transport of substances;

- eliminating waste substances through the liver and kidneys.

Therefore, maintaining proper hydration levels is crucial for preserving Total Body Water (TBW) [13]: the baseline quantity of water required to achieve this is around 2 liters for adult women and 2.5 liters for adult men [14]. The regulation of total

body water is highly precise, maintaining a continuous balance between intake and loss. Under normal metabolic conditions, a dynamic equilibrium is sustained, with approximately 2 liters of water being replaced every 24 hours [15].

During physical activity, body heat is dissipated through sweat, a substance primarily composed of water and minerals. During moderate physical activity, sweat production is approximately 100 ml/hour, which can reach a value of 3 L/hour during intense and prolonged physical activity in a very hot and humid environment. This results in a decrease in Total Body Water (TBW) with negative consequences on the body, including cardiovascular fatigue, hyperthermia, reduced performance (physical and cognitive), cramps, and in extreme cases, death. To prevent overheating, the heat generated during physical activity must be partially dissipated in order to maintain a stable internal temperature. There are several mechanisms for lowering body temperature [1]:

- conduction: immersing the body in cold water;

- radiation: when heat is radiated away from the body;

- convection: air moving around the body helps reduce its temperature;

- Evaporation: sweat droplets evaporate, carrying away heat.

Among these, evaporation is the most efficient cooling mechanism for the human body.

## 1.3.1   Body temperature regulation

The human body's thermoregulatory mechanisms are primarily responsible for maintaining the temperature of the central volumes of the body (including the brain, abdomen and thoracic cavity) at approximately 37 degrees Celsius [1].The termoregulation center of the body is located in the hypothalamus, which regulates thermal dispersion and termogenesis. The hypothalamus receives information regarding the body's internal temperature from thermoreceptors situated near the internal organs. It also receives data about the external environment's temperature from peripheral thermoreceptors present in the skin (Figure 1.17)[1].

The human body is unable to regulate skin temperature; however, it is responsive to external stimuli, prompting the adoption of certain behaviors, such as covering oneself when exposed to cold temperatures.

In a hot environment, the body implements various strategies to reduce its temperature. The vasodilation of the blood vessels in the skin enables the body to dissipate a portion of its energy through the conduction effect. When this is insufficient the evaporation effect is then initiated by the evaporation of sweat produced by the sweat glands [1].
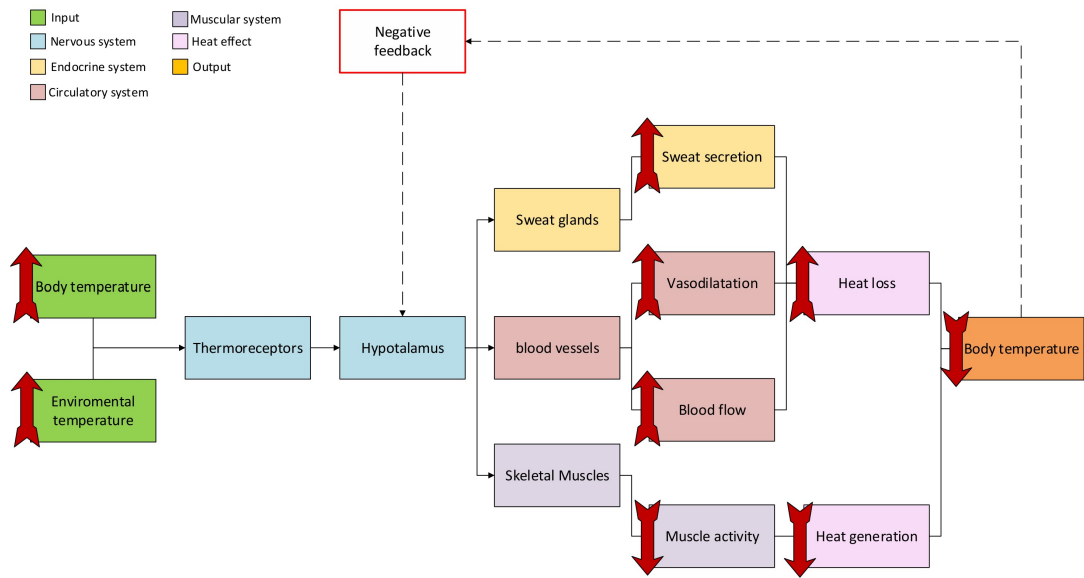
**Figure 1.17:** *Diagram onf the body's responses to temperature rising.*

However, cutaneous vasodilation becomes an ineffective thermoregulation mechanism when the external temperature exceeds the internal one, while sweating is less efficient in conditions of high environmental humidity.

In order to regulate the body's internal temperature, it is essential to maintain optimal water concentration in the body, which is regulated by the thirst center.the thirst center (Figure 1.18) located in the hypothalamus, where osmoreceptors detect changes in the osmolarity of intracellular fluid. In cases of hyperosmolarity, the thirst reflex is triggered, prompting the individual to drink. Additionally, the secretion of antidiuretic hormone (ADH) reduces renal water excretion [15] [16].
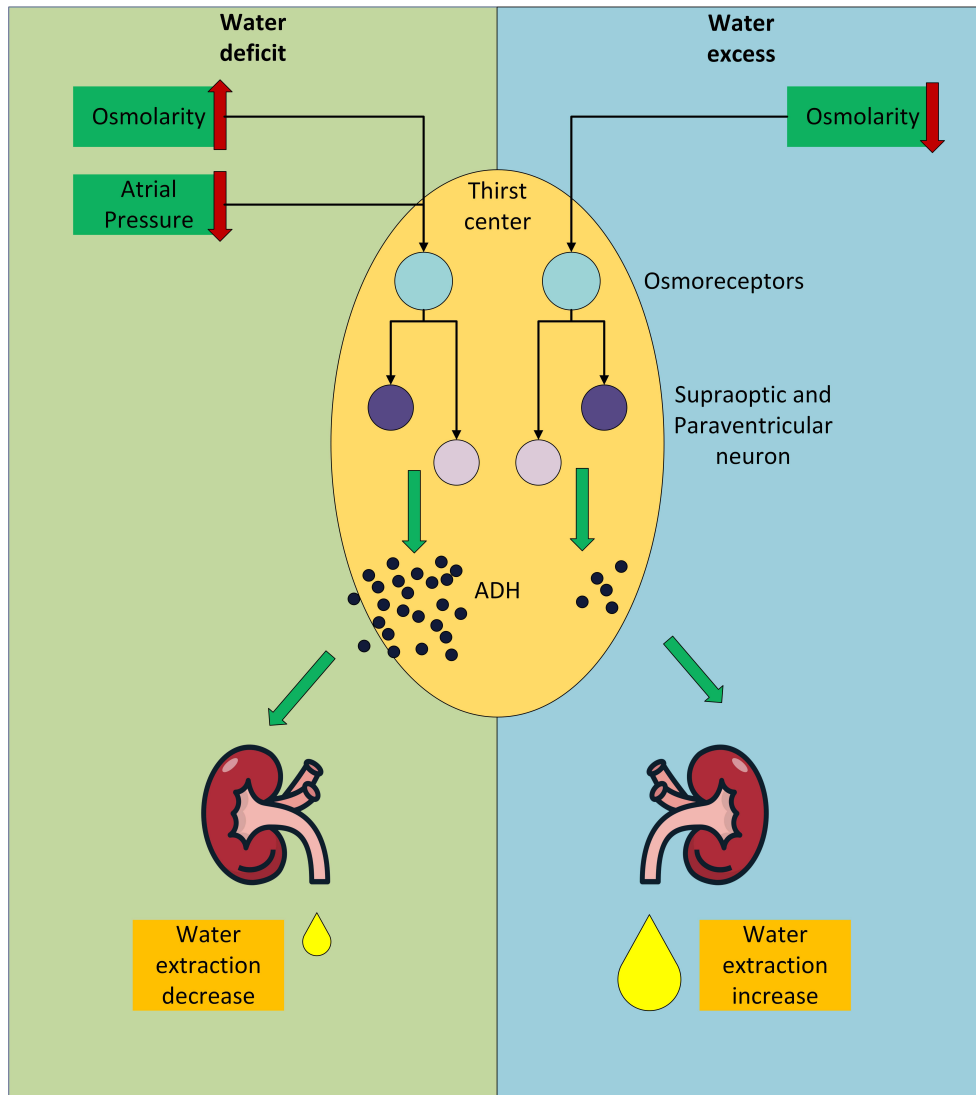
**Figure 1.18:** *Thirst Control Center: in the absence of water, osmolarity increases and atrial pressure decreases. ADH is produced and the kidney produces less urine. In case of excess water, osmolarity decreases, less ADH is produced, and the kidney produces more urine.*

The sensation of thirst does not occur immediately when dehydration begins but rather at a later stage, once the process is already underway; therefore, waiting for the sensation of thirst to rehydrate is not a reliable strategy for maintaining adequate fluid balance [15]. The delay between thirst sensation and begin of dehydration is due to the fact that the thirst sensation is not entirely accurate and is influenced by various factors, including psychological ones.

The function of sweat glands in thermoregulation is very important and they can be classified into two main categories:

1. eccrine glands are distributed throughout the body, with a higher concentration in the forehead, palms, and footplate. These glands secrete sweat, which contains high levels of chloride and sodium, through pores in the skin;

2. the apocrine glands are primarily located in the axillary area and the anogenital region. They secrete sweat through the hair follicle, with a high concentration of chloride and sodium, similar to the previous glands. However, in addition to these substances, they also release sweat with protein and fatty acids.

The two glands exhibit a response to the body temperature and the activity of the sympathetic nervous system [1].

## 1.3.2   Water movement inside the sweat glands

The process of sweating is initiated by the release of hormones from the thermoregulation center, which stimulate the activity of sweat glands as seen before. These glands absorb water and other substances from the plasma that composed the 55% of blood [17]. Actually that the plasma is composed of 90% water and contains electrolytes, proteins, and nutrients that are absorbed or not based on the type of sweat gland [1].
Before being secreted, sweat passes through the eccrine gland channel where the electrolytes present are actively reabsorbed through the membrane [17]. This results in an osmotic pressure differential between the sweat within the duct and the surrounding liquid, which is composed of a higher electrolyte concentration. Some of the water is then reabsorbed within the body as a result of the osmosis process (Figure 1.19 ). The water is partially reabsorbed within the body by osmosis. The rate of reabsorption is dependent upon the rate of exit. In the presence of intense heat, the rate of exit is increased, resulting in a reduction in the amount of water reabsorbed [1] [17].
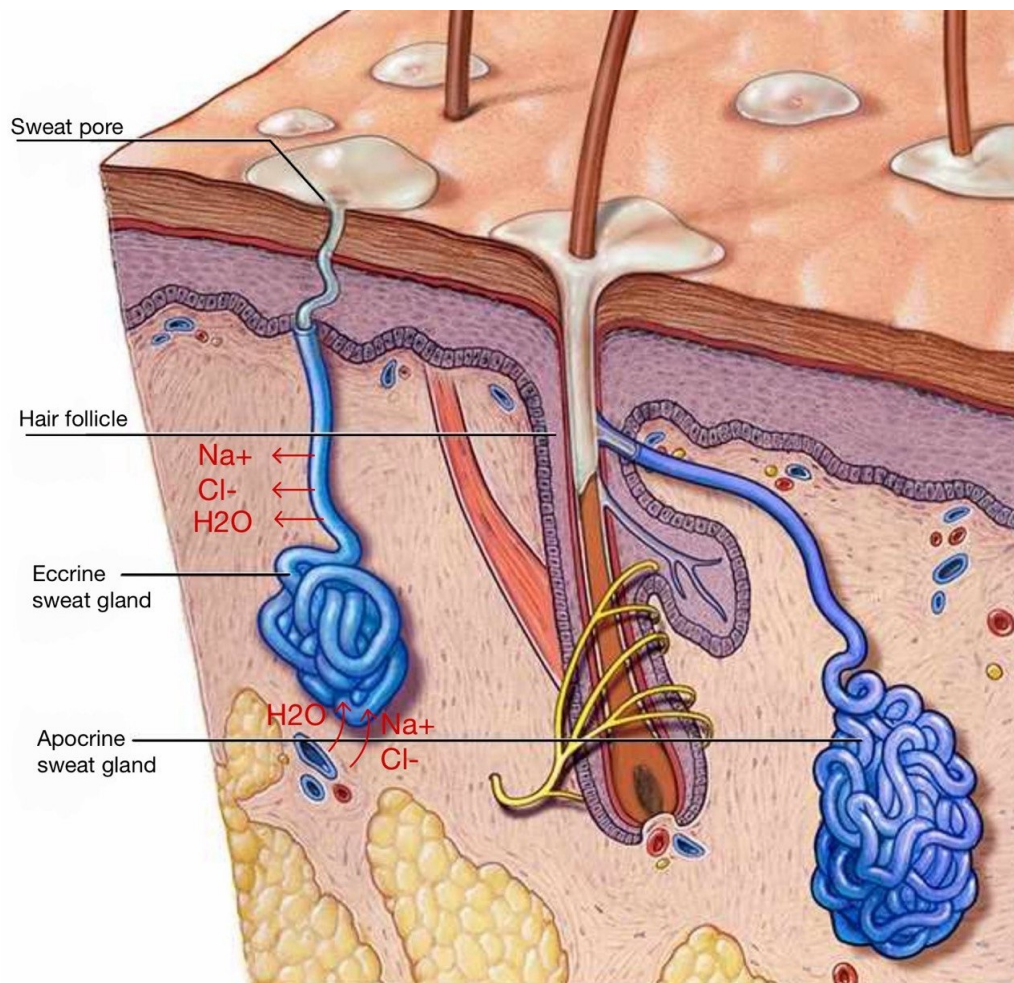
**Figure 1.19:** *Sweat glands positioning and substances exchange with adjacent tissues.*

## 1.3.3 Mechanisms of water absorption and distribution in the human body

The water we ingest follows a multi-step process before reaching the bloodstream. First, it enters the stomach, where some preliminary absorption takes place, though most of it remains unabsorbed at this stage. Next, the water passes into the small intestine, which is lined with millions of small, finger-like projections called villi. These villi increase the surface area for absorption, facilitating the passage of water and nutrients through the intestinal walls. Through a process called osmosis, water molecules move from the cells of the intestine into the capillaries within the villi, entering the bloodstream. From there, water is distributed throughout the body,

supplying all cells and tissues that require it (Figure 1.20). The kidneys play a key role in regulating this water balance by filtering the blood, removing excess water, and retaining necessary amounts based on the body's needs [1].
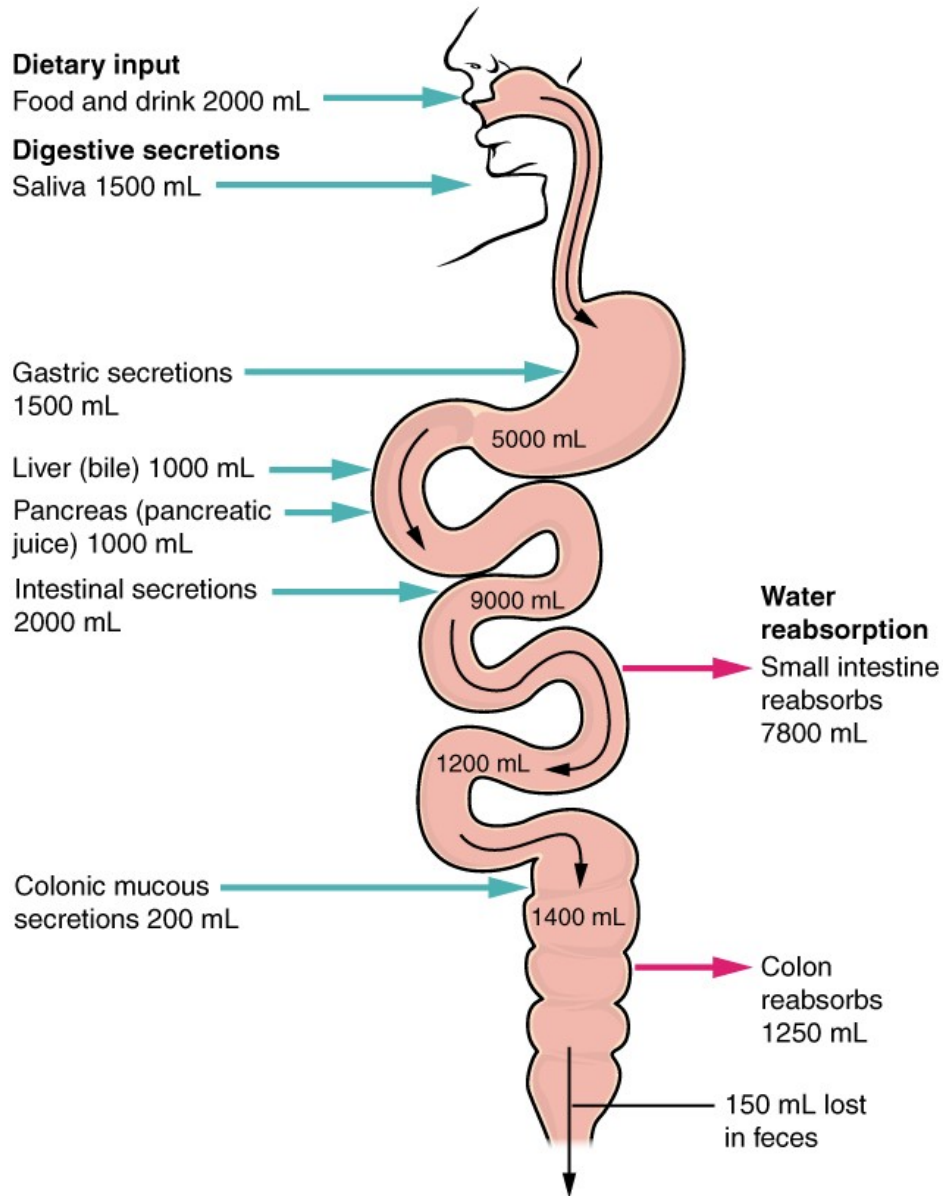


**Figure 1.20:** *Water absorption. Thanks to osmosi water flow from small intestine to bloodstream.*

# Chapter 2

# Principles of ultrasound imaging

## 2.1 Physics of ultrasound and anatomy of the ultrasound machine

The ultrasound image results from the interaction of high-frequency sound waves with the tissues of the human body [18]. Frequencies commonly used in ultrasound range from 1 to 10 MHz. These sound waves are emitted by the ultrasound probe and propagate through body tissues, interacting with various structures. Snell's law, which describes the reflection and refraction of sound waves as they pass from one tissue to another (Figure 2.1), is fundamental to interpreting the ultrasound image [19]. It can be written as:

$$\eta_1 \cdot sin(\alpha) = \eta_2 \cdot sin(\gamma) \tag{2.1}$$

where:

- $\eta_1$ and $\eta_2$ are refractive indices;

- $\alpha$ is the angle of incidence;

- $\gamma$ is the angle of refraction.

This law helps us understand how sound waves are reflected from different surfaces, such as the various anatomical structures in the human body: some tissues, such as bones, have a very high acoustic impedance and reflect a good portion of the incident wave, while others have a low acoustic impedance and transmit the wave.
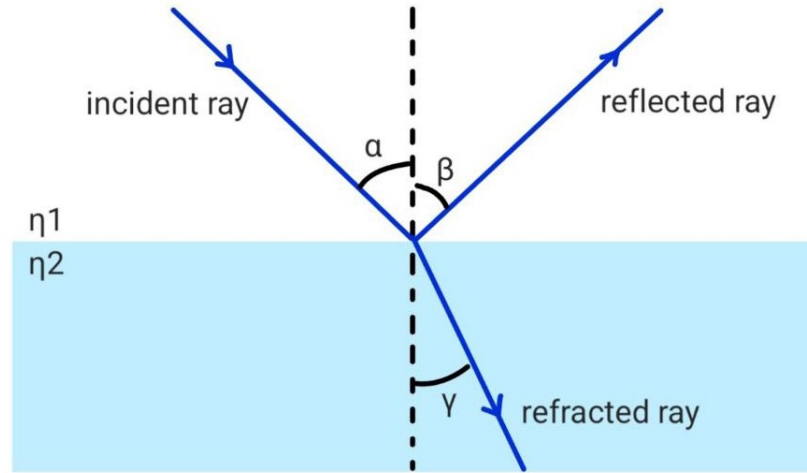
**Figure 2.1:** *Snell's law representation.*

The frequency of sound waves is crucial for image resolution: at higher frequencies, the ultrasound machine can produce images with higher resolution, which are ideal for superficial or detailed structures. However, as the scanning depth increases, the frequency of sound waves must decrease to penetrate deeper into tissues [19].
The speed of sound in biological tissues is approximately 1540 meters per second (m/s) and it depends by the density and the elasticity of it, In particular, the rate of propagation will be greatest in dense, non-elastic tissues such as bone ($v = 4080m/s$) and least in soft tissues such as lipid-rich adipose tissue ($v = 1460m/s$) [19]. The speed of wave is described by:

$$v = \lambda \cdot f \tag{2.2}$$

where:

- $v$ is the velocity of sound waves in a specific tissue;

- $\lambda$ is the wavelength;

- $f$ is the frequency of the wave.

Lambda also represents the theoretical axial resolution, beyond which smaller details cannot be observed. However, in commercial devices, the ultrasound machine does not emit a single cycle of a sine wave but rather a packet of duration T composed of 3 or 4 sinusoidal cycles; in practice smaller details cannot be appreciated beyond the length of the transmitted packet [19].
The most important property of the tissue is the acoustic impedance ($Z$), it describe the resistance that a sound wave find during the propagation in a tissue [19].

It is directly proportional to the density ($\rho$) of the given tissue and the speed ($v$) of sound within it:

$$Z = \rho \cdot v \tag{2.3}$$

The unit of measurement used is the Rayl equal to $\frac{\text{Kg}}{\text{m}^2 \cdot \text{s}} \cdot 10^6$ [19]. The acoustic impedances of tissues within the body exhibit a range between 1.38 Rayl of adipose tissue and 1.62 Rayl of kidney [19]. Exceptions to this can be observed in the lungs, which have a very low acoustic impedance due to their air filling, and in bones, which have a very high acoustic impedance due to their density [19].

The ultrasound machine consists of several key components essential for imaging. At its core is the ultrasound generator, responsible for producing high-frequency electrical signals. These signals are then sent to the PZT (Lead Zirconate Titanate) crystal within the probe. The PZT crystal is a crucial element that exhibits the direct and inverse piezoelectric effect. When an electrical signal is applied, the crystal vibrates, generating ultrasound waves through the direct piezoelectric effect [19]. Conversely, when ultrasound waves strike the crystal, it produces electrical signals due to the inverse piezoelectric effect, which are then used for imaging [19]. The probe, equipped with the PZT crystal, is placed on the skin and emits ultrasound waves into the body.

The generated wave propagates through the body until it reaches the interface between two tissues with different acoustic impedances ($Z_1$ and $Z_2$). From Snell's law (2.1), it can be demonstrated that the incident wave is divided into two components: the transmitted (T) and the reflected (R) wave [19]. When an incident wave is perpendicular to the tissue interface, the resulting reflect coefficient is simplified to:

$$R = \left( \frac{Z_1 - Z_2}{Z_1 + Z_2} \right)^2 \tag{2.4}$$

It can be observed that the most energy is transmitted when the acoustic impedence difference is close to zero; however, when the acoustic impedence differences are significantly greater, the reflect coefficient is close to one, causing the wave to return competitively [19]. The ultrasonographic wave is not transmitted unaltered within the tissues; rather, it attenuates due to energy dissipation in the tissue. The amplitude then decays in accordance with an exponential trend, as follows [19]:

$$A(x) = A_0 \cdot e^{-\alpha x} \tag{2.5}$$

where:

- $A(x)$ is the amplitude of the wave at distance x from the origin;

- $A_0$ is the amplitude of the original wave;

- $\alpha$ is the absorption coeficient, it is a propriety of the tissue and it depends also by the frequency of the wave (higher the frequency the higher the absorption).

To rectify the discrepancy in amplitude readings, ultrasonographic devices employ a technique known as Time Gain Compensation (TGC), another important feature, it is designed to produce images with balanced brightness. The echoes returning from deeper structures are weaker than those from superficial structures. To selectively enhance the weaker echoes the operators can adjust the amplification of signals based on depth, compensating for attenuation in deeper tissues, attenuating the brightness of the superficial field and increasing that of the deeper field [19]. The TGC works as a logarithmic amplifier, as a matter of fact (2.5) is exponential, calculating depth (h) as:

$$h = \frac{1}{2} \cdot v \cdot t \tag{2.6}$$

where $t$ is fly time of the sound wave (delay between emitted wave and echos returned) while $v$ is the wave speed.

## 2.2 Echocardiography and imaging of IVC

Generally, to obtain good images of the inferior vena cava, a convex probe formed by PZT sensors arranged along a circumference radius is used (Figure 2.2).



**Figure 2.2:** *Convex probe by Telemed medical systems s.r.l.*

The frequencies employed reach up to 5 MHz, allowing the detection of the vein located at a depth of approximately three centimeters under the skin.

Ultrasound imaging of blood vessels can be performed using two modes (Figure 2.3):

- B-mode, where the brightness of the displayed image is directly related to the amplitude of the returning echoes, while the position corresponds to the depth at which these echoes originate. In this mode, the ultrasound probe is typically positioned at the top of the monitor, with the depth increasing toward the bottom of the image [18];

- M-mode: is used in conjunction with B-mode to examine pulsatile structures and qualitatively assess the movement of the walls over time. The resulting traces display depth on the vertical axis and time on the horizontal axis. The image is oriented so that the ultrasound probe appears at the dorsal part of the image [18].
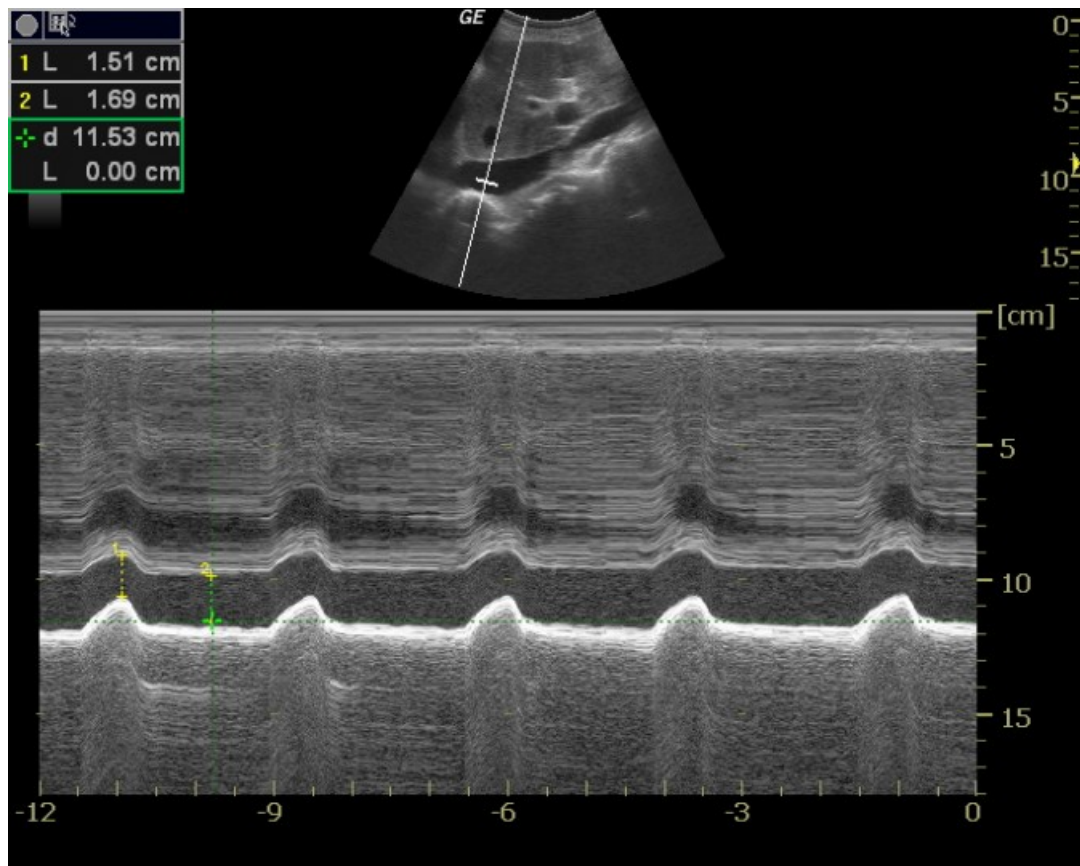


**Figure 2.3:** *On the top the B-mode acquisition and on the bottom the M-mode acquisition.*

The portion of the inferior vena cava of interest can be studied in different views: the transverse in Figure 2.4 and the longitudinal in Figure 2.5. To do this, the probe must be positioned correctly on the subject's skin, in a sub-sternal position, orienting it according to a reference marker placed on the probe itself that identifies the direction of the view [20].
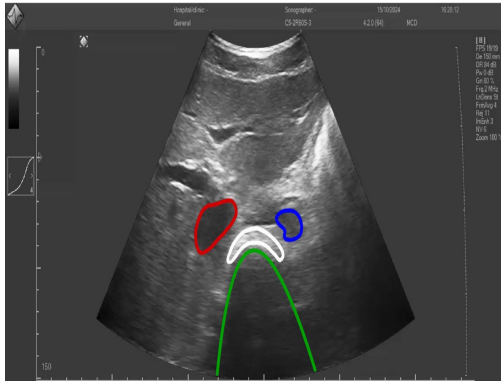


**Figure 2.4:** *IVC trasversal view. In blue the IVC, in red the aorta, in white hyperecoic vertebral body, in green the shadow generated by the vertebral body.*
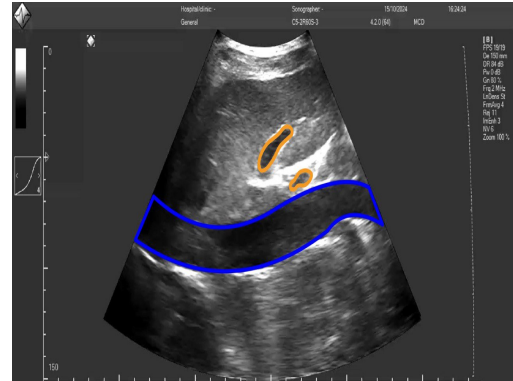


**Figure 2.5:** *IVC longitudinal view. IVC in blue, two hepatic veins in orange.*

# Chapter 3

# State of the Art on Hydration and the Role of the Inferior Vena Cava

Dehydration occurs due to fluid loss during physical exertion. As sweat evaporates, it cools the skin and blood, helping to lower the body's internal temperature. However, once dehydration sets in, the body can no longer cool itself effectively. When a significant amount of fluid is lost during physical activity and not properly replaced, the internal body temperature rises, and the sweating process becomes impaired due to the reduced water reserves. At this stage, feelings of fatigue emerge, leading to a decline in physical, athletic, and cognitive performance [21].
It is estimated that a weight loss equivalent to 1% of body weight results in an increase of 0.4 C° in internal temperature and in a decrease approximately of 2-3% in physical efficiency [22]. Additionally, for every liter of sweat lost, heart rate increases by approximately 8 beats per minute, while cardiac output decreases by about 1 liter per minute [23].

## 3.1   State of the Art on Hydration study

To monitor the hydration status, body weight and urine are usually assessed, particularly its concentration, volume, osmolality, and color. Regarding body weight, changes in body mass are a precise indicator of water loss: it is assumed that following physical activity, the change in weight is solely due to fluid loss through sweating and that a one-gram change corresponds to one milliliter of lost water [13]. A widely used parameter in clinical practice is the ratio of blood urea nitrogen (BUN) to serum creatinine, which proves to be a highly sensitive parameter

[24]. Another method is measuring urine specific gravity, as a higher concentration of solutes in urine typically signifies dehydration. Similarly, evaluating urine osmolality provides insights into hydration levels, with elevated values suggesting dehydration. Blood plasma osmolality is another critical measure; increased concentrations of solutes in blood plasma are associated with dehydration [25]. Additionally, skin turgor can be assessed qualitatively by examining the elasticity of the skin, while bioelectrical impedance analysis (BIA) estimates body composition, including total body water, by measuring the resistance to electrical flow through the body. These methods for assessing hydration status are simple and non-invasive, but they require time, laboratory analysis and instruments with good sensitivity to accurately evaluate fluid loss variation. The methods mentioned are summarized in the Table 3.1.

**Table 3.1:** Methods for assessing hydration status.

| Method | Parameter Assessed | Description |
|---|---|---|
| **Body Weight** | Body mass changes | Monitors weight before and after physical activity to estimate fluid loss, assuming $1g \approx 1mL$ water. |
| **Urine Analysis** | Concentration, volume, osmolality, color | Measures various urine characteristics; higher solute concentrations typically indicate dehydration. |
| **Blood Urea Nitrogen (BUN) / Serum Creatinine Ratio** | BUN-to-creatinine ratio | Common clinical parameter; elevated BUN/creatinine ratio is sensitive to hydration status changes. |
| **Urine Specific Gravity** | Solute concentration in urine | Higher specific gravity (more concentrated urine) is a sign of dehydration. |
| **Urine Osmolality** | Solute concentration in urine | Increased osmolality in urine indicates lower hydration levels. |
| **Blood Plasma Osmolality** | Solute concentration in blood plasma | Higher plasma osmolality correlates with dehydration. |
| **Skin Turgor** | Skin elasticity | Qualitative measure; decreased elasticity can signal dehydration. |
| **Bioelectrical Impedance Analysis (BIA)** | Total body water | Estimates body composition, including total body water, based on electrical resistance. |

## 3.2 Study of IVC during dehydration in athletes

In several studies [3] [26] [27], it was considered to utilize ultrasonographic images of the inferior vena cava to assess hydration status, based on its diameter and pulsatility index (CI). The parameters calculated on the IVC in hydrated and dehydrated subjects were correlated with the BUN/creatinine values: specifically, in dehydrated subjects (BUN/creatinine ratio >20), the CI index was higher compared to hydrated subjects (BUN/creatinine ratio <20), and the diameter at end-expiration was lower [27] [28]. Another study [3] shows that in dehydrated individuals, the vein appears to have a smaller diameter compared to more hydrated individuals; moreover, in hypovolemic subjects, pulsatility tends to be higher. In the study [29] conducted by Anna L. Waterbrook and colleagues, the main objective was to determine whether sonographic measurement of the inferior vena cava (IVC) diameter in college football players during preseason camp was a reliable method to detect and monitor dehydration. The researchers hypothesized that IVC diameter measurements, the post-practice caval index, and expiratory diameter were significantly related to percent weight loss after preseason football practice. The sample consisted of Division I intercollegiate football players participating in preseason training camp. Sonographic IVC measurements were obtained using both the subcostal and subxiphoid approaches during inspiration and expiration, both before and after a practice of approximately 3 hours with moderate to high levels of exertion and high ambient temperatures. Results showed a significant relationship between post-practice expiratory IVC diameter ($R^2 = 0.153$, $p = 0.042$) and percent weight loss after practice, with IVC diameter significantly inversely correlated with percent weight loss ($R^2 = -1.07$). However, the post-practice caval index was not found to be significantly correlated with weight loss ($R^2 = 0.078$, $p = 0.16$). Another study [30] aimed to assess the diameter of the inferior vena cava in 23 marathon runners, specifically evaluating the maximum and minimum diameters of the vein before and after the marathon.

The results showed a statistically significant difference ($p = 0.004$) in the maximum diameter measurements taken prior to and following the physical activity, alongside the corresponding fluid loss due to sweating. Moreover, the study shows a statistically significant negative correlation between weight loss with maximum diameter of the IVC ($p = 0.047$) before and after the run.

The study conducted by Kristofer Hedman et al. [31] confirms that trained individuals have larger IVC dimensions compared to untrained subjects ($p < 0.01$): this allows for a significant blood influx to the muscles involved in the activity without excessively increasing pressure, which is detrimental to the body. It is crucial, therefore, to know the training status of the subject in order to draw meaningful conclusions about the reduction in inferior vena cava dimensions following dehydration.

# Chapter 4

# Methodology and Experimental Protocol

## 4.1 Purpose of the study and expected results

The principal objective of this study is to examine the potential correlation between dehydration and specific parameters calculated on the inferior vena cava (IVC) in healthy subjects. Another aim of this study is to analyze and measure variations in the IVC's physiological behavior in response to dehydration, focusing on changes every 10 minutes of physical activity and their relationship with parameters, for example like heart rate (HR).

## 4.2 Materials

The systems for acquiring the data necessary for the study are:

- a Reharunner 02 treadmill, manufactured by Chinesport S.p.A., Italy. The walking parameters can be set via the onboard computer, allowing adjustment of belt speed and incline. The device is powered from the mains (220-240 V, 15 A, 50-60 Hz), with a maximum power consumption of 2000 W. The maximum permitted speed is 25 km/h, while the maximum incline is +30%;

- a G&G PSE-150 scale with a capacity of 150 kg and a resolution of 10 g for weights below 50 kg, or a resolution of 20 g for weights above 50 kg. The device is powered by batteries. The parameter displayed on the screen is the weight of the subject;

- a heart rate sensor (Polar H10) for obtaining an ECG signal derivation. The device is powered by a CR 2025 battery and can be connected to mobile devices via 2.4 GHz Bluetooth Smart. It operates in a range of temperatures between -10 °C and +50 °C. The sensor should be positioned below the chest in frontal part of the body;

- an application (Polar Sensor Logger), available only for Android, to real-time visualization of the parameters recorded by the Polar band and for the local data storage;

- an open architecture ultrasound device, MicrUs Ext-1H, developed by Telemed. The system can be connected to a PC via USB port and supports various types of probes. For the study, a convex probe C5-2R60S-3 by Telemed medical systems s.r.l. was used, which can be utilized in different imaging modes, including B mode and M mode. The probe crystals are of type S3, and the transducer can operate in the frequency range of 2-5 MHz. It has a curvature radius of 65 mm and a field of view of 60°;

- an ultrasound system management software, ECHO WAVE II (version 4.3.0), which allows the management of the ultrasound system. The software has a user interface with customizable settings and programmable buttons that enable measurements and calculations on the ultrasound frame of interest. It allows saving of photographs and videos in various formats.

## 4.3 Experimental protocol

### 4.3.1 Test execution

To ensure that the subjects of the study were in the most homogeneous conditions possible, they were asked to maintain adequate hydration by consuming at least two liters of water and refraining from smoking and alcohol intake on the day preceding the test execution. Ultimately, the subjects were instructed to present themselves in a fasting state for a minimum of two hours. Additionally, the preceding meal was to be light and easily digestible, in order to prevent excessive blood flow to the digestive organs located near the IVC. This could potentially alter the dimensions of the inferior vena cava or impede its visualization through ultrasound, given the dilation and filling of the stomach that occurs after a meal. To minimize the

amount of perspiration remaining on the clothing, which could affect the accuracy of the weight measurements, the subjects were instructed to wear shorts. The male participants were instructed to remove their shirts, while the female participants were to wear sports tops.

The participants in the study underwent a test involving the acquisition of images of the inferior vena cava before and after performing a moderate-intensity physical activity, throughout the entire task, participants wore a heart rate monitor that recorded the ECG, acceleration along the three axes, and heart rate. In particular, the protocol consists of:

1. initial weighing: the subject, after dressing as indicated above, wears the Polar H10 band so that it is always present in weight measurements and is weighed without shoes and socks. data on weight, height, and weekly training hours were finally saved in a database;

2. baseline definition of the IVC: prior to the start of physical activity, an ultrasound video in longitudinal view was conducted to establish the baseline condition of the IVC;

3. settle down: the subject has 1 minutes to wear shoes and prepare for the task;

4. physical activity: Participant engaged in a 10-minute walk on a treadmill set at a 10% incline and a speed of 5 km/h. During the session the subjects were instructed to dry themselves frequently to remove sweat and prevent absorption by clothing, which could have affected the overall weight;

5. sweat drying: in order not to weigh down the sweat, the subject was asked to dry himself off really well;

6. weighing: subsequently, the subject was weighed without shoes in order to ascertain the quantity of water lost during the exercise session through perspiration;

7. IVC imaging: following the physical activity, another ultrasound video in longitudinal view was performed to assess any changes in the size of the IVC.

The last five steps are repeated 5 times for a total of physical activity of 50 minutes. Following the conclusion of the final repetition, the hydration session should be initiated:

8. hydration: The subject should consume an amount of water equivalent to that which is lost during the course of the physical activity;

9. wait for absorption: The subject is required to wait for a period of two minutes, during which time the water is to be absorbed;

10. IVC imaging: A longitudinal ultrasound video was conducted to evaluate potential alterations in the dimensions of the IVC.

The last two steps of the hydration session were also repeated 3 times in order to allow the vena cava to return to the starting size assessed during the baseline. It was assumed that the weight loss was solely due to the loss of water (with a ratio of 1 gram lost per every milliliter of water lost) expelled through sweat (according to [30]), as participants were unable to change clothes or use the restroom during the activity.

The entire timeline of the protocol is illustrated in figure 4.1:



**Figure 4.1:** *Experimental protocol timeline. A) dehydration phase, B) rehydration phase.*

## 4.3.2 Positioning the probe

The probe used for ultrasound imaging acquisition was positioned subcostally, at the level of the lower edge of the heart rate monitor, maintaining the same position for all acquisitions to study the same portion of the vein consistently. Additionally, the hepatic vein was utilized as an internal reference for the subject, allowing for the analysis of the same portion of the IVC between the tasks. Finally, the reference on the probe was oriented towards the subject's face so that what is located in the upper body was represented on the right side of the image.

**Figure 4.2:** *Probe positioning for longitudinal view.*



**Figure 4.3:** *Probe positioning for trasversal view.*

## 4.4 Methods

### 4.4.1 Dataset

The study sample consists of 37 healthy voluntary subjects: 18 females and 19 males, aged between 19 and 29 years (median = 24, 24 ± 1.92). The average height is 170.68 ± 8.47 cm, and the average weight is 65.1 ± 12.4 kg. Each subject was asked about the number of hours of physical activity performed during the week and the type of activity. On average, the participants engaged in 3.18 ± 2.94 hours of physical activity per week. Notably, 9 subjects reported no physical activity, while 2 subjects practiced sports at a competitive level.

Seven subjects were excluded from the dataset: five subjects were excluded due to difficulties in extracting the IVC diameter, which was not clearly identifiable in the video; two subjects were excluded due to problems in saving the Polar band data, leaving 30 subjects for later data analysis.
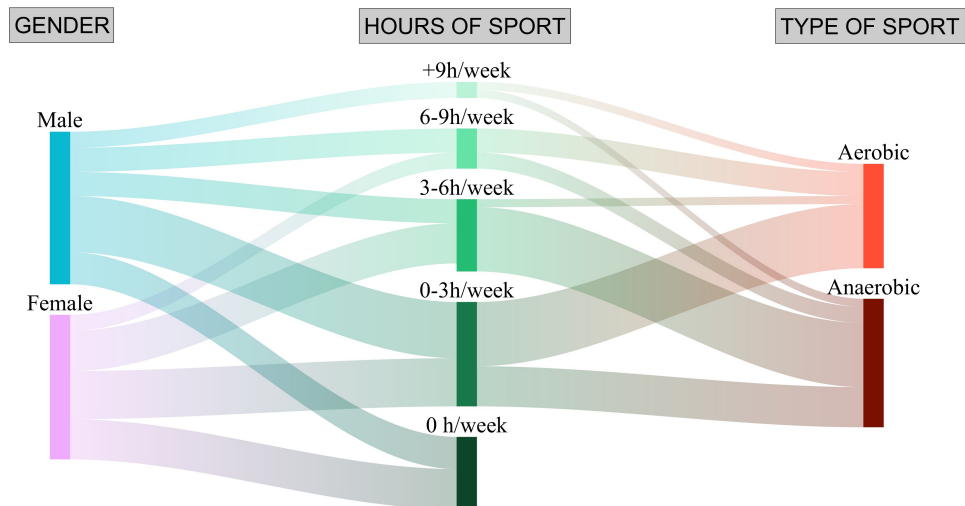


**Figure 4.4:** *Dataset division considering participants' gender, their weekly training hours and the type of sport practiced.*

### 4.4.2 Telemed software

For the acquisition of videos of the inferior vena cava, the Telemed software was employed, offering the possibility to configure different acquisition modes depending on the specific needs of the study. In particular, the B-mode acquisition was chosen to evaluate the pulsatility of the venous district according to [18]. The ability to modulate the scanning depth, an important feature of the software, allowed precise adjustments tailored to each subject. The scanning depth was determined

based on the anatomical characteristics of each individual, considering both the depth of the vein and the abdominal wall's thickness. For subjects with varying body compositions, different depths were set to obtain optimal imaging, with scanning depths ranging from 120 to 180 millimeters, depending on the individual's abdominal thickness and adipose tissue layer. This customization ensured accurate visualization of the vein's characteristics for each case.

Another critical parameter that was configured is the focus depth. Even though some subjects may appear physically similar in terms of abdominal width and the thickness of the adipose tissue layer, the position of the vein can vary significantly in depth. In certain individuals, the vein was located quite superficially, while in others, it was found in a much deeper region.

This variability in vein positioning made it essential to adjust the focus depth appropriately. Ensuring that the focus area was precisely aligned with the region of the vein being examined was fundamental to obtaining clear and detailed images. This adjustment allowed the analyzed section of the vein to be clearly visible in the acquired video, improving the quality of the visualization.

The gain parameter was also adjusted, which plays a key role in influencing the return signal and, as a result, affects the overall brightness of the video being acquired. The gain setting has a global impact on the intensity of the returning echoes, regulating the brightness of the ultrasound image by amplifying or attenuating the signal from all depths within the scanned area. This adjustment is crucial because it ensures that both superficial and deeper structures are clearly visible, allowing for a balanced and consistent visualization of the anatomical features being studied.

Lastly, the dynamic range was configured, a parameter that significantly influences the contrast within the ultrasound image. By adjusting the dynamic range, it is possible to alter the grayscale representation, either expanding or compressing the range of gray tones in the image. This adjustment allows for a more precise visualization of anatomical structures that have varying acoustic impedances, which might otherwise appear blended or indistinguishable due to similar echogenic properties.

The software provides the functionality to save the acquired video in a user-defined format, and for the purposes of this study, the .mp4 format was selected. The frame rate depends on the selected scanning depth: as the scanning depth increases, there is a corresponding decrease in the frame rate. This is because deeper structures require more time for the ultrasound waves to travel and return to the probe, thereby affecting the speed at which frames can be captured.

This inverse relationship between scanning depth and frame rate needs to be taken into account, particularly when comparing subjects with varying anatomical depths. Despite the lower frame rate for deeper scans, the videos still provided sufficient temporal resolution to accurately assess the physiological characteristics of the

inferior vena cava. In the recorded videos, the sampling frequency varied from 16 fps to 20 fps. In order to achieve the target of recording at least three respiratory cycles, 399 frames were recorded, which, in the worst case scenario of 20 fps, would allow for approximately 20 seconds of video to be captured.

### 4.4.3   Diameters and CI extraction

The inferior vena cava (IVC) was traced from the recorded videos using software provided by VIPER.srl and implemented in MATLAB. During the initial stage, the software provides the option to select the starting and ending frames of the video that will undergo processing. This functionality is particularly useful as it allows the exclusion of video sections where the inferior vena cava may not be clearly visible. By focusing only on the frames in which the vein is well-defined and clearly visible, this feature ensures that the subsequent tracking process is not compromised. This software offers the capability to select two high-contrast points within the first frame of the video, which serves as reference points for the tracking process. That is necessary because movements may occur during the video that do not keep the vein in the position of the first frame, caused, for example, by breathing; this improves diameter estimation by allowing the vein's movements to be followed. Additionally, the software allows the user to define the upper and lower boundaries of the vein on the left side of the screen, ensuring accurate delineation of the vein's structure. A line can then be drawn to indicate the end of the section of the vein that is to be tracked, effectively marking the portion of interest for further analysis (Figure 4.5).

As a result, a video is produced that includes the detailed tracking of the portion of the inferior vena cava selected for analysis. The software precisely outlines the region of interest, with the upper and lower borders of the vena cava marked in red to ensure clear visualization throughout the video (Figure 4.6).

Furthermore, the software provides a framework that contains the start frame, the end frame selected and the x and y coordinates of each point of the upper and lower edge of the vein for each frame of the video.

After the tracking data is acquired, the VIPER software generates the diameters of the inferior vena cava. The software processes the x and y coordinates of the inferior vena cava borders that were previously calculated and uses these to compute the mean line. It is derived by averaging the corresponding points from the upper and lower borders of the vein. The averaged points are then interpolated using a second-degree polynomial fit, creating a smooth representation of the vein's mean line. From this interpolation, the exact coordinates of the mean line are obtained. Following the interpolation, the software calculates the length of the mean line from the initial point to the final point in pixel units, as the physical dimensions of the pixels are not provided. The user can choose to exclude a percentage of the
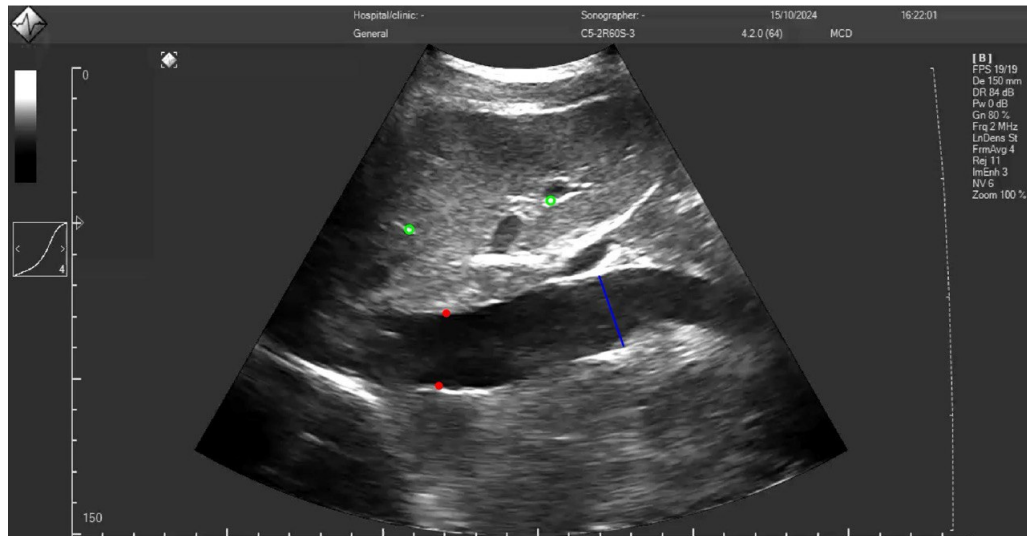
**Figure 4.5:** *Two green circles indicate the high-contrast reference points selected by the user, while the two red dot marks the upper and lower edges of the vein. The blue line on the right delineates the right end section of the vein to be tracked.*
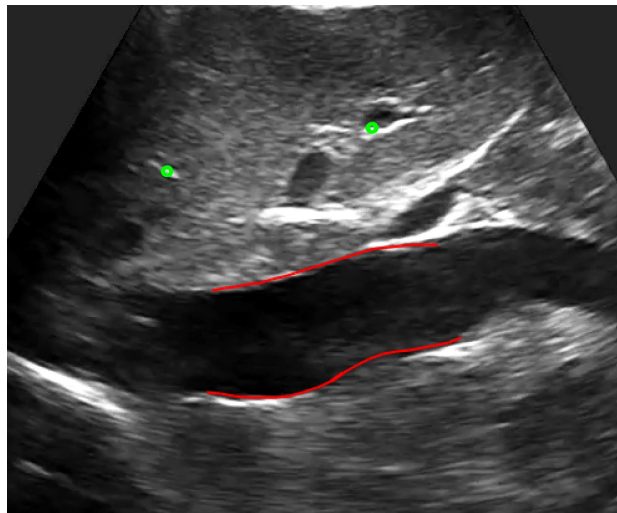


**Figure 4.6:** *In green the reference points selected by the user, in red are the lines delineating the IVC, drawn by the software.*

total length of the edges in order to eliminate sections with less precision from the analysis due to instabilities caused by interpolation: it was decided to eliminate 10% on the right and 10% on the left. Additionally, the software allows the user to select the number of points or lines used for analysis, 21 being selected for our studies according to [32]. For each video frame, these points are uniformly distributed

along the remaining mean line (80% centered). At each of the selected positions, 21 perpendicular lines evenly distributed in the selected portion of the vein are drawn from the mean line to intersect with the vein's upper and lower borders. These perpendicular intersections provide the necessary data to compute the vein's diameter at each position. For each frame, 21 diameter values are obtained, which are then averaged to produce a single value for each video frame (Figure 4.7).
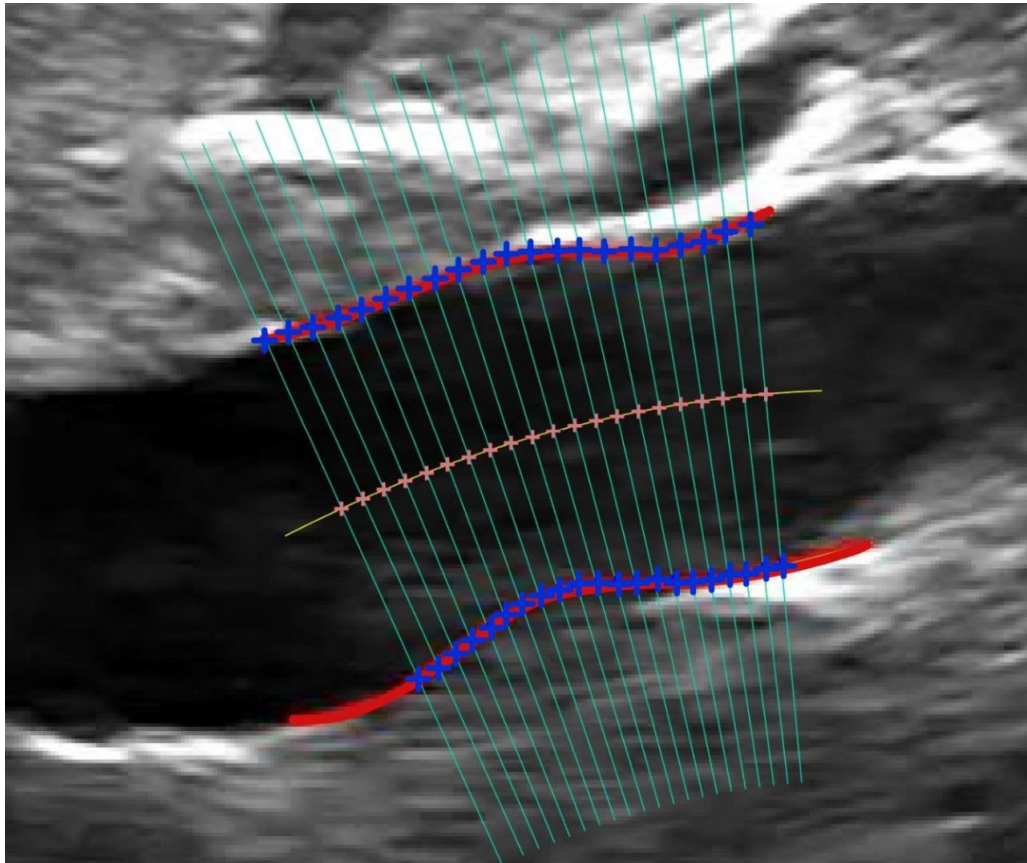


**Figure 4.7:** *Single frame illustrates diameters extraction: red lines represent the walls of the IVC; yellow line shows the interpolation with a parabola of the mean line; pink crosses are the 21 equidistant points from which the desired diameters represented in light blue originate.*

The diameters calculated from the ultrasound data were initially expressed in pixels, making it necessary to convert these pixel-based measurements into millimeters to ensure accurate and meaningful results.

This conversion is crucial for comparing the values with standard reference measurements in the medical field. To accomplish this, the depth of each ultrasound video was carefully evaluated. In particular, the user is asked to select a distance

of 50 mm on an ultrasound frame. To do this, the sidebar shown in Figure 4.8 is used, where each tick mark corresponds to 10 mm. Based on this depth, a specific conversion factor was derived for each individual case, which was then applied to transform the diameters from pixel units into millimeters [33] [34].
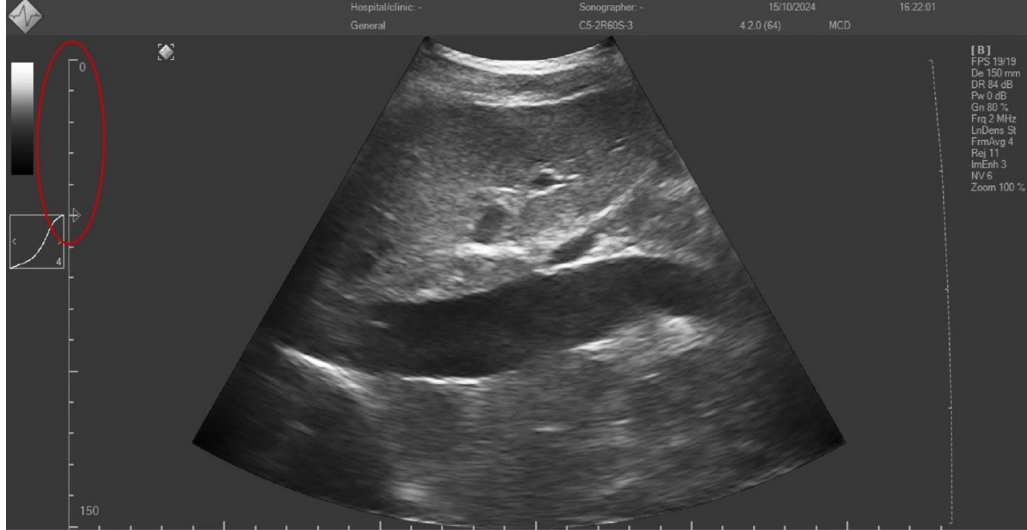


**Figure 4.8:** *On the left the bar, each tick mark corresponds to 10 mm.*

At this stage, the diameter is calculated [35]; the variation in diameter throughout the video is influenced by two components: the respiratory component, characterized by low-frequency oscillations, and the cardiac component, which exhibits higher-frequency fluctuations [32],[36].

$$D_{\text{tot}} = D_{\text{resp}} + D_{\text{cardiac}} \tag{4.1}$$

In order to extract these components the mean diameter values undergo several filtering processes. In particular, to isolate the respiratory component is employed a low-pass filter with a cutoff frequency at 0.4 Hz, while to isolate the cardiac component, a high-pass filter with a cutoff frequency of 0.8 Hz has been used [32]. Subsequently, the caval index (CI) is calculated based on the diameter value, the cardiac caval index (CCI) is determined from the cardiac component, and the respiratory caval index (RCI) is derived from the respiratory component. To calculate the caval indices (Figure 4.9), the maximum and minimum peaks of the respective components were calculated and locate the corresponding values in the original diameter signal, after the maximum and minimum values of the respective components were interpolated: in this way, the CCI and RCI were obtained according to the formula (1.3) Using interpolation of maximums as $max(D)$ and interpolation of minimums as $min(D)$ [32].
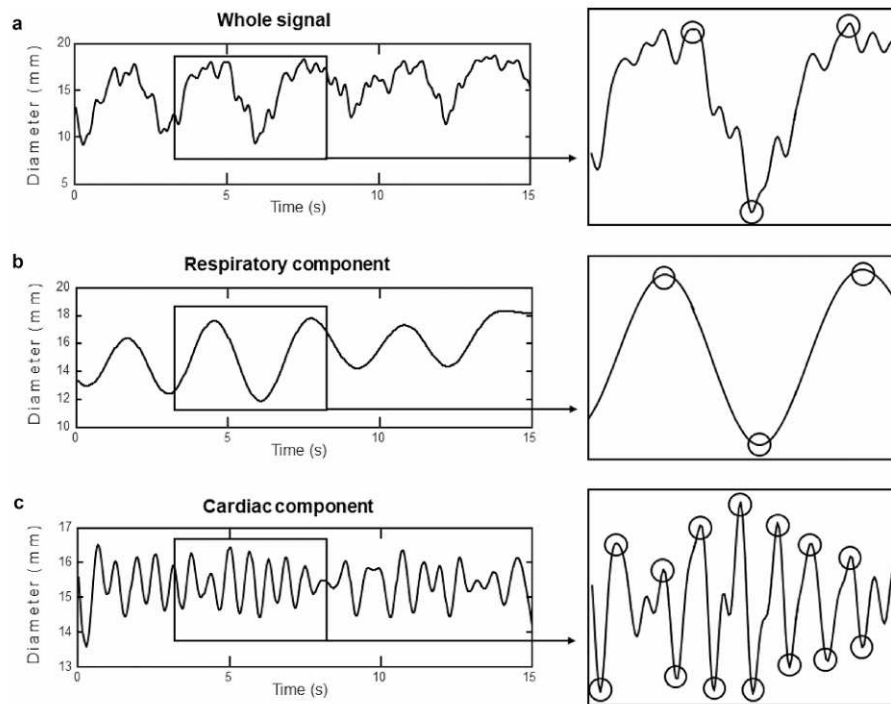
**Figure 4.9:** *a) Whole diameter signal and the extimation of CI b) Respiratory component and extimation of RCI c) Cardiac component and extimation of RCI.*

These measurements are taken for each ultrasound scan: prior to physical activity, during breaks from physical activity, and during hydration periods.

The process involves capturing data at these specific intervals to provide a comprehensive analysis of the inferior vena cava's response to different physiological conditions.

### 4.4.4 Analysis of operator and VIPER software repeatability

To evaluate the repeatability of the operator who performed the ultrasound scans and extracted the parameters using the software, a protocol was established for obtaining ultrasound images under resting conditions. Subjects were asked to maintain a supine position for 10 minutes to allow blood redistribution and ensure that the vein maintained a consistent diameter across all measurements. Subsequently, four successive videos of the inferior vena cava (in a longitudinal section) were recorded, which were later processed with the VIPER software to obtain diameter measurements.

Repeatability assessment was conducted on 11 subjects. For each video, median

diameter values were obtained, along with the standard deviation of the four median values for each subject [37],[38]. Also, the intraclass correlation coefficient (ICC) was calculated and depens on two parameters: mean square between subjects ($MS_B$) and mean square within subjects ($MS_S$), calculated as follow:

$$MS_B = \frac{1}{N-1} \sum_{i=1}^{N} k \cdot (\bar{D}_i - \bar{D})^2 \tag{4.2}$$

$$MS_W = \frac{1}{N(k-1)} \sum_{i=1}^{N} \sum_{j=1}^{k} (D_{ij} - \bar{D}_i)^2 \tag{4.3}$$

$$ICC = \frac{MS_B - MS_W}{MS_B + (k-1) \cdot MS_W} \tag{4.4}$$

where:

- k is the number of observations for subjecrs;

- N is the number of subjects;

- $\bar{D}_i$ is the mean of the diameters of the i-th subject;

- $\bar{D}$ is the mean of all diameters;

- $D_{ij}$ j-th diameter of the i-th subjects.

### 4.4.5 Analysis on significant differences

From the Viper software, we obtained a vector of diameters and caval index (CI) for each ultrasound trial. From these, we extracted the following:

- the average value is calculated as the mean of the vector;

- the maximum value is obtained by identifying the peaks of the vector and calculating their median;

- The minimum value is obtained by identifying the valley of the vector and calculating their median.

This approach allowed us to obtain more robust estimates that are less affected by potential outlier errors. To study significant differences between the various trials, we performed outlier removal, identifying outliers as values exceeding three times the median absolute deviation (MAD), calulated as:

$$MAD = \text{median}(|X_i - \text{median}(X)|) \tag{4.5}$$

where X is the distribution and $X_i$ is the single value inside the distribution. Next, we tested the normality of the data distribution for the baseline phase and each subsequent trial using the Shapiro-Wilk test. Based on the distribution type, we investigated whether there was a statistically significant difference in diameter and CI values obtained during the dehydration and rehydration phases. Specifically, we compared the baseline to each trial up to 50 minutes (dehydration phases) and the 50-minute trial to each trial up to 6 minutes post-rehydration (rehydration phase). To examine these differences, we used two statistical tests: the t-test for normally distributed variables and the Wilcoxon test for non-normally distributed variables.

### 4.4.6 Analysis of trends in dehydration and rehydration phases

For the analysis of trends within the dehydration and rehydration phases, all subjects were considered separately. For each subject, the average diameter was taken into account, as this parameter showed a significant difference in both the dehydration and rehydration phases when analyzing the sample, as will be shown later in the Figure 5.3. The average diameter values for each subject were linearly interpolated to obtain two slope coefficients ($m$) for each subject, one for dehydration and one for rehydration.

$$D = m * t + q \tag{4.6}$$

Thanks to that, it was possible classified the subject based on the angular coeffcient they have in the two differet phase:

- $m_{dehydrated} < 0 \land m_{rehydrated} > 0$ : this is the optimal scenario, where the IVC diameter decreases during dehydration and increases during rehydration;

- $m_{dehydrated} < 0 \land m_{rehydrated} < 0$ : in this instance, the dehydration follows the hypothesized trend, yet the rehydration does not;

- $m_{dehydrated} > 0 \land m_{rehydrated} > 0$ : in this instance, the rehydration follows the hypothesized trend, yet the dehydration does not;

- $m_{dehydrated} > 0 \land m_{rehydrated} < 0$ : in this scenario, the angular coefficient exhibits a trend that is contrary to the hypothesized one.

In order to avoid angular coefficients close to zero, which are therefore not significant, subjects were classified separately if they have angular coefficients that met the following condition:

$$m < 0.1 * |mean(m)| \tag{4.7}$$

The angular coefficients were related to the percentage of mean bpm during walking trial with respect to the maximum bpm, calculated in 1.4.

The same linear interpolation was performed on the sample medians to obtain the general trend.

Interpolation 4.6 was also used on the difference between the trial diameters and the baseline diameters to determine the time required for the vena cava to return to its original dimensions: in particular when during the rehydration phase $\Delta D$ return to 0 mm.

$$t^{rehydrated} = \frac{-q}{m} \tag{4.8}$$

## 4.5 Classification of subjects based on correct and incorrect Trends: a k-NN Model

To determine whether it was possible to classify subjects with trends consistent with the literature (decreasing dehydration and increasing rehydration), the k-Nearest Neighbors (k-NN) method was applied. A k-NN model was built for each trial starting from all the 21 available variables (shown in Table 4.1). To identify the best performance, a grid search method was implemented to optimize the number of neighbors (k), the distance metric used and the threshold to identify which variables are considered correlated. The evaluated k values range from 1 to 70, and the distance metrics considered include Euclidean, city block, cosine, correlation, and Minkowski distances. Various thresholds ranging from 0 to 1, in steps of 0.01, were tested. The leave-one-out method was adopted for performance evaluation, which involves removing the variables of one subject at a time, training the model with the remaining subjects, and classifying the removed subject. Subsequently, to identify variables that could be removed due to redundancy and lack of informational contribution, the accuracy of the k-NN model was evaluated by varying a threshold while fixing the distance metric and the value of k that yielded the best performance. For each trial, the threshold that resulted in the highest accuracy was applied to the correlation matrix of the 21 variables. Based on this analysis, a subset of variables was selected to optimize the classification of the two subject groups. In this way, after n minutes of training, it is possible to identify the variables that best distinguish subjects with the expected trend from those with a different trend.

**Table 4.1:** *Variables taken into account for the linear model construction, delta are expressed as a percentage.*

| Name | Meaning |
|---|---|
| $\Delta W$ | weight variation between baseline and single trial |
| $\Delta D_{mean}$ | mean diameter variation between baseline and single trial |
| $\Delta D_{max}$ | maximum diameter variation between baseline and single trial |
| $\Delta D_{min}$ | minimum diameter variation between baseline and single trial |
| $\Delta D_{std}$ | standard deviation of diameters variation between baseline and single trial |
| $\Delta HR_{mean\_eco}$ | variation of the mean heart rate between baseline and ultrasound exam |
| $\Delta HR_{max\_eco}$ | variation of the maximum heart rate between baseline and ultrasound exam |
| $\Delta HR_{min\_eco}$ | variation of the minimum heart rate between baseline and ultrasound exam |
| $\Delta HR_{std\_eco}$ | standard deviation of heart rate variation between baseline and ultrasound exam |
| $\Delta CI_{mean}$ | mean caval index variation between baseline and single trial |
| $\Delta CI_{max}$ | maximum caval index variation between baseline and single trial |
| $\Delta CI_{min}$ | minimum caval index variation between baseline and single trial |
| $\Delta CI_{std}$ | standard deviation of caval index variation between baseline and single trial |
| $\Delta CCI_{mean}$ | mean cardiac caval index variation between baseline and single trial |
| $\Delta CCI_{max}$ | maximum cardiac caval index variation between baseline and single trial |
| $\Delta CCI_{min}$ | minimum cardiac caval index variation between baseline and single trial |
| $\Delta CCI_{std}$ | standard deviation of cardiac caval index variation between baseline and single trial |
| $\Delta RCI_{mean}$ | mean respiratory caval index variation between baseline and single trial |
| $\Delta RCI_{max}$ | maximum respiratory caval index variation between baseline and single trial |
| $\Delta RCI_{min}$ | minimum respiratory caval index variation between baseline and single trial |
| $\Delta RCI_{std}$ | standard deviation of respiratory caval index variation between baseline and single trial |

## 4.6 Evaluation of a predictive linear model for rehydration time based on dehydration phase

To examine the possible correlation between the rehydration time of each subject and the dehydration phase, a linear model was developed. The model was built considering the subjects who exhibit a decreasing trend during the dehydration phase and an increasing trend during the rehydration phase (15 subjects). Furthermore, their baseline diameter is higher than the diameter measured at the end of dehydration, resulting in a positive diameter variation at the start of the rehydration phase.

The dependent variable chosen for the model was the time required to return to baseline values during the rehydration phase, expressed in minutes. The model takes into account the physiological parameters of each subject for each trial: five linear models were then constructed, starting from the 10-minute trial up to the 50-minute trial. To select the most relevant parameters to include in the model, a correlation analysis of the 21 available variables of the 14 subjects with correct trend was performed to identify correlated variables and exclude them from the final model evaluation. To determine the threshold above which two variables are considered correlated and one should be excluded, an approach was adopted using different correlation thresholds, ranging from 0 to 1 in steps of 0.001. Five models were thus built, one for each trial, and their performance was evaluated in terms of:

1. the coefficient of determination $(R^2)$, which measures the proportion of variance explained by the model and calculated as:

$$R^2 = 1 - \frac{\text{SSE}}{\text{SST}} \tag{4.9}$$

where SSE is the sum of squared error and SST is the sum of squared total;

2. the mean squared error (MSE), which quantifies the average deviation between observed and predicted values.

In this way, a threshold value was obtained for each trial considering the minor MSE, enabling the selection of the most informative variables for each case. This approach allows for the estimation of rehydration time, taking into account the different training durations.

# Chapter 5

# Results

## 5.1 Repetibility

The repeatability analysis show that the operator with the software achieved a mean standard deviation of 0.94 mm and an ICC (calculated as show in 4.4) value of 0.946. Table 5.1 provides detailed measurements of the diameter across the four videos of IVC for each subject, with the respective standard deviations.

**Table 5.1:** *Diameters value of the four repetitions (D1 to D4) and standard deviation expressed in mm.*

| Subject | D1 | D2 | D3 | D4 | STD |
|---------|------|------|------|------|------|
| S01 | 0.94 | 1.24 | 1.10 | 1.03 | 1.3 |
| S02 | 1.17 | 0.88 | 1.14 | 1.01 | 1.3 |
| S03 | 2.21 | 2.24 | 2.12 | 2.17 | 0.54 |
| S04 | 0.79 | 1.07 | 1.10 | 0.91 | 1.4 |
| S05 | 1.03 | 1.01 | 0.97 | 0.89 | 0.61 |
| S06 | 1.08 | 1.22 | 1.10 | 1.21 | 0.72 |
| S07 | 1.17 | 1.04 | 0.99 | 0.95 | 0.99 |
| S08 | 1.46 | 1.42 | 1.38 | 1.18 | 1.2 |
| S09 | 1.39 | 1.60 | 1.47 | 1.45 | 0.87 |
| S10 | 1.65 | 1.95 | 1.83 | 1.71 | 1.3 |
| S11 | 0.61 | 0.67 | 0.67 | 0.59 | 0.41 |

## 5.2  Analysis of significant differences

The baseline is normally distribuited for all considered parameters: mean diameter (Table 5.2), maximum diameter (Table 5.3), minimum diameter (Table 5.4), mean CI (Table 5.5), maximum CI (Table 5.6) and minimum CI (Table 5.7) where analyzed. In particular the tables indicate whether there are significant differences between the baseline distribution and the distributions observed after each walking trial (dehydration phase) and if there are significant difference between the last trial and each phase of rehydration.

**Table 5.2:** *Distribution and significativity of mean diameter values.*

| Trial | Distribution | Significant difference | $p$-value |
|-------|--------------|------------------------|-----------|
| 10 min | Not gaussian | No | 0.36 |
| 20 min | Gaussian | No | 0.34 |
| 30 min | Not gaussian | No | 0.19 |
| 40 min | Gaussian | No | 0.16 |
| 50 min | Gaussian | Yes | **0.019** |
| post 2 | Gaussian | No | 0.56 |
| post 4 | Not gaussian | No | 0.16 |
| post 6 | Not gaussian | Yes | **0.028** |

**Table 5.3:** *Distribution and significativity of maximum diameter values.*

| Trial | Distribution | Significant difference | $p$-value |
|-------|--------------|------------------------|-----------|
| 10 min | Gaussian | No | 0.07 |
| 20 min | Gaussian | No | 0.36 |
| 30 min | Not gaussian | No | 0.14 |
| 40 min | Gaussian | No | 0.18 |
| 50 min | Gaussian | Yes | **0.014** |
| post 2 | Gaussian | No | 0.73 |
| post 4 | Not gaussian | No | 0.14 |
| post 6 | Gaussian | Yes | **0.03** |

**Table 5.4:** *Distribution and significativity of minimum diameter values.*

| Trial | Distribution | Significant difference | *p*-value |
|---|---|---|---|
| 10 min | Not gaussian | No | 0.16 |
| 20 min | Not gaussian | No | 0.43 |
| 30 min | Gaussian | No | 0.27 |
| 40 min | Gaussian | No | 0.31 |
| 50 min | Gaussian | No | 0.06 |
| post 2 | Gaussian | No | 0.46 |
| post 4 | Gaussian | No | 0.16 |
| post 6 | Gaussian | Yes | **0.0062** |

**Table 5.5:** *Distribution and significativity of mean CI values.*

| Trial | Distribution | Significant difference | *p*-value |
|---|---|---|---|
| 10 min | Gaussian | No | 0.90 |
| 20 min | Gaussian | No | 0.63 |
| 30 min | Gaussian | No | 0.80 |
| 40 min | Not gaussian | No | 0.75 |
| 50 min | Gaussian | No | 0.93 |
| post 2 | Not gaussian | No | 0.77 |
| post 4 | Gaussian | No | 0.99 |
| post 6 | Gaussian | No | 0.23 |

**Table 5.6:** *Distribution and significativity of maximum CI values.*

| Trial | Distribution | Significant difference | *p*-value |
|---|---|---|---|
| 10 min | Gaussian | No | 0.76 |
| 20 min | Gaussian | No | 0.58 |
| 30 min | Gaussian | No | 0.97 |
| 40 min | Gaussian | No | 0.77 |
| 50 min | Gaussian | No | 0.86 |
| post 2 | Gaussian | No | 0.77 |
| post 4 | Gaussian | No | 0.56 |
| post 6 | Gaussian | No | 0.51 |

**Table 5.7:** *Distribution and significativity of minimum CI values.*

| Trial | Distribution | Significant difference | *p*-value |
|-------|--------------|------------------------|-----------|
| 10 min | Gaussian | No | 0.97 |
| 20 min | Gaussian | No | 0.79 |
| 30 min | Gaussian | No | 0.78 |
| 40 min | Not gaussian | No | 0.71 |
| 50 min | Gaussian | No | 0.99 |
| post 2 | Not gaussian | No | 0.61 |
| post 4 | Gaussian | No | 0.44 |
| post 6 | Gaussian | No | 0.32 |

In Figure 5.1 the distributions of mean, maximum, and minimum diameter are displayed. In particular values during the baseline, after physical activity, and at the end of the rehydration phase are taken into account. The absolute values of the diameter variation are shown in Table 5.8.
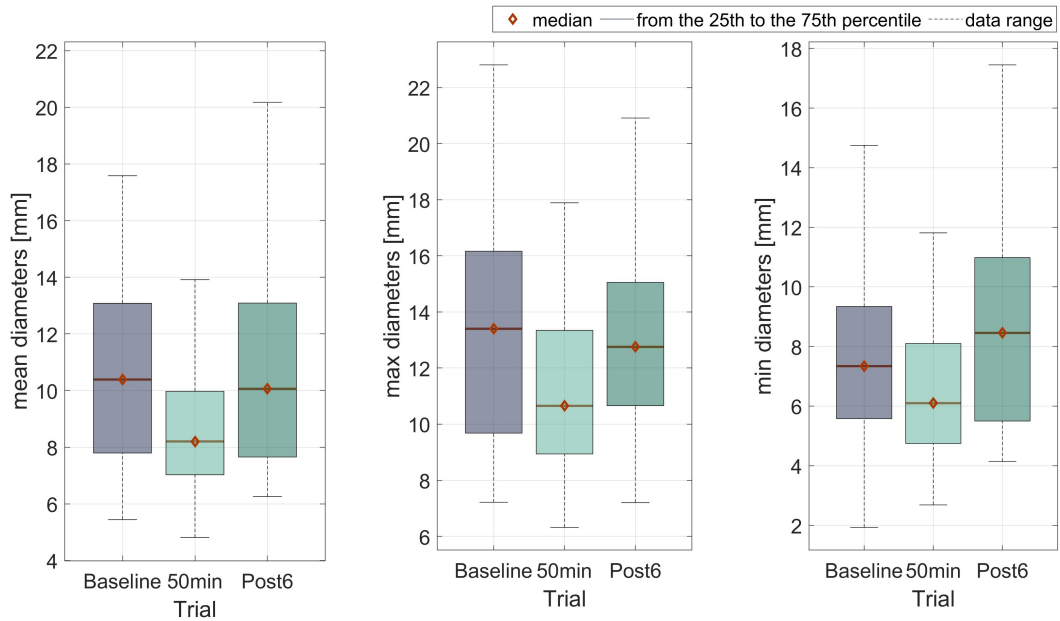


**Figure 5.1:** *Significant differences between baseline, 50 min and post 6. A) values of mean diameter, B) values of maximum diameter, C) values of minimum diameter.*

**Table 5.8:** *Median values of parameter in trial and respective variations during dehydration and rehydration phases.*

| Parameter | Value [mm] | $\Delta D$ [mm] |
|---|---|---|
| D mean | Baseline = 10.39 <br> 50 min = 8.20 <br> Post 6 = 10.06 | Dehydration = 2.19 <br> Rehydration = 1.86 |
| D max | Baseline = 13.40 <br> 50 min = 10.65 <br> Post 6 = 12.75 | Dehydration = 2.75 <br> Rehydration = 2.1 |
| D min | Baseline = 7.34 <br> 50 min = 6.1 <br> Post 6 = 8.46 | - <br> Rehydration = 2.5 |

In Figure 5.2, the distributions of the caval index (mean, maximum, and minimum) are shown in baseline conditions and at the end of dehydration and at the end of the rehydration phase. It can be observed that there is no difference between the median value of the three distributions.
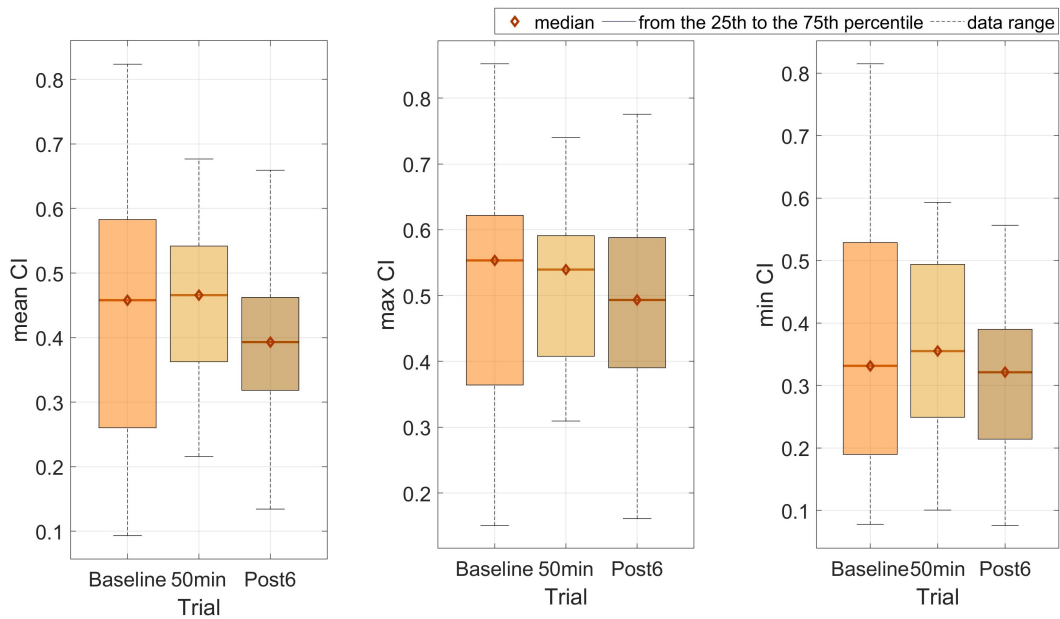


**Figure 5.2:** *Significant differences between baseline, 50 min and post 6. A) values of mean CI, B) values of maximum CI, C) values of minimum CI.*

## 5.3 Trends

### 5.3.1 Overall trends of diameter and CI

The results show a progressive decrease in the mean diameter from baseline values up to 50 minutes; subsequently, during the rehydration phase, an increase is observed (Figure 5.3).The total angular coeficient of the sample is equal to:

- $m_{deydration}$ = -0.036 mm/min

- $m_{reydration}$ = 0.197 mm/min
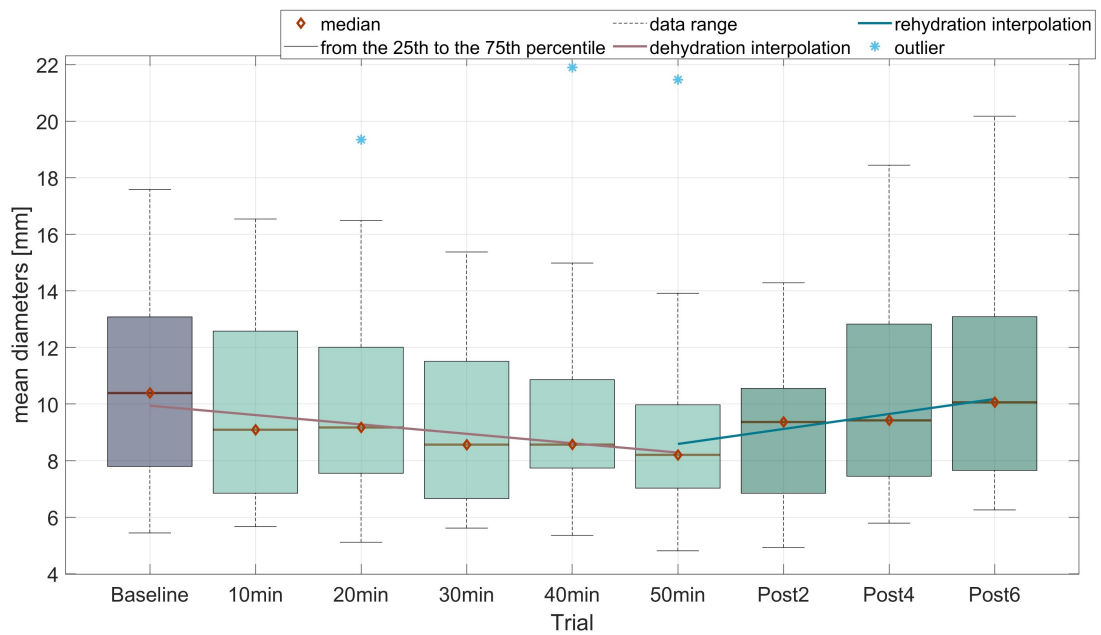


**Figure 5.3:** *Trend of mean diameter during dehydration phase (from Baseline to 50 min) and rehydration phase (from 50 min to Post6).*

The mean caval index values remain constant during the dehydration phase and show a slight decrease during the rehydration phase (Figure 5.4).
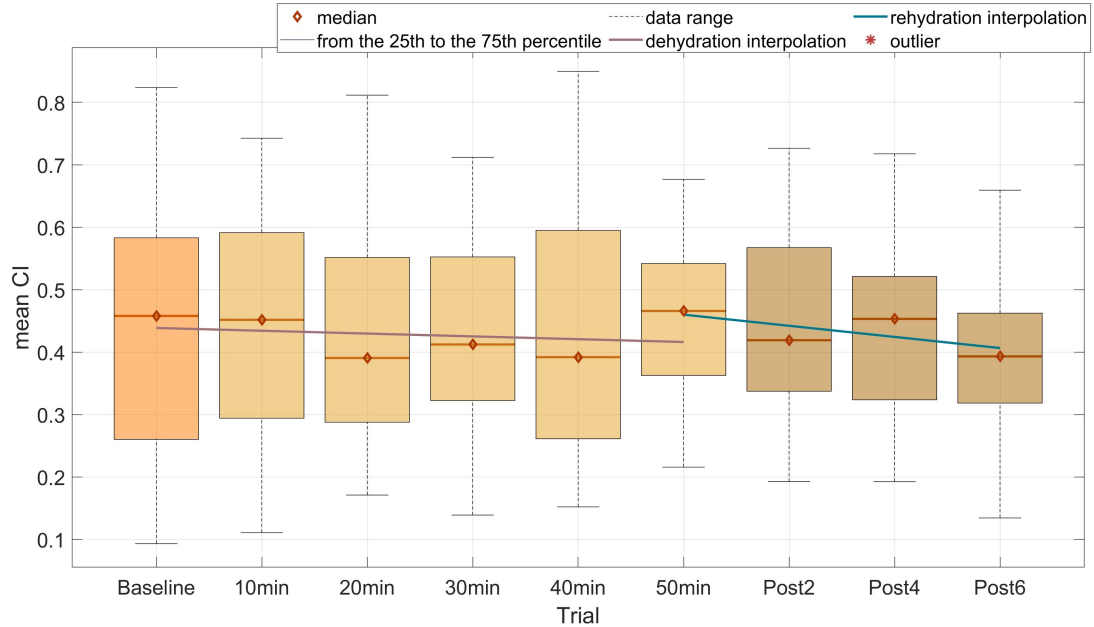


**Figure 5.4:** *Trend of mean caval index (CI) during dehydration phase (from Baseline to 50 min) and rehydration phase (from 50 min to Post6).*

## 5.3.2 Subjects trends of diameter

The angular coefficients of individual subjects are shown in Figure 5.5. The gaussianity of the two distribution was evaluating by Shapiro-Wilk test, which returned that both distributions are normal, with a standard deviation of 0.046 mm/min for dehydration and 0.37 mm/min for rehydration as shown in Table 5.9. Finally, significant differences were checked with a t-test that returned a p-value of 0.0001. The Figure 5.6 shows the angular coefficients of the dehydration (A) and rehydration (B) phases as a function of bmp percentage. Two thresholds are highlighted: the first represents the aerobic threshold, and the second represents the anaerobic threshold. Specifically, one subject is below the aerobic threshold, while four are above the anaerobic threshold. On the right, a confusion matrix (C) displays the number of subjects who exhibit the trends analyzed during the two phases (4.4.6).
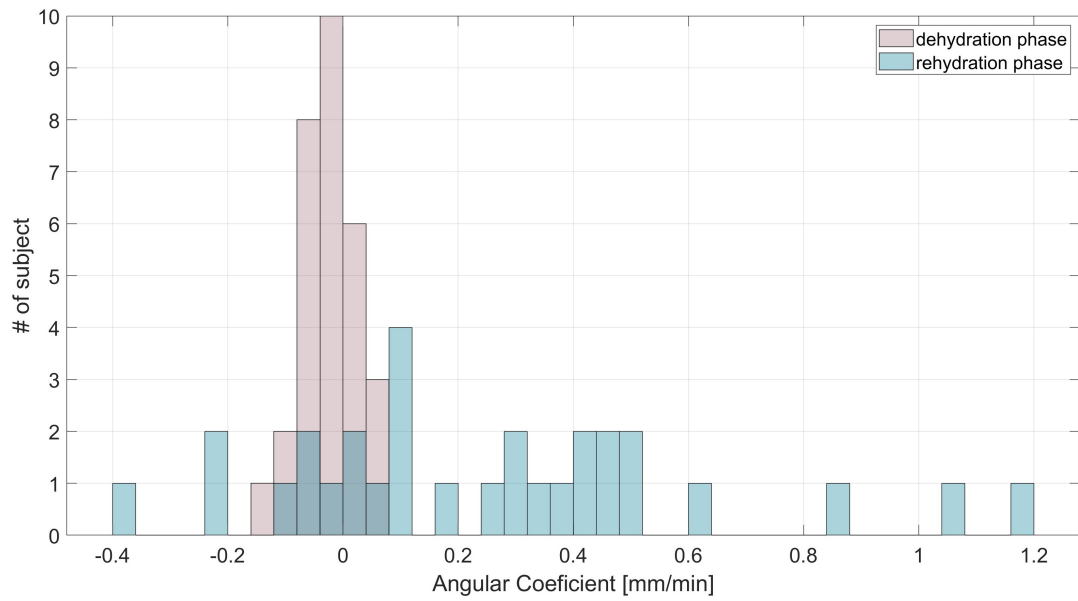
**Figure 5.5:** *Distribution of angular coefficient in dehydratoion phase (pink) and rehydration phase (blue).*
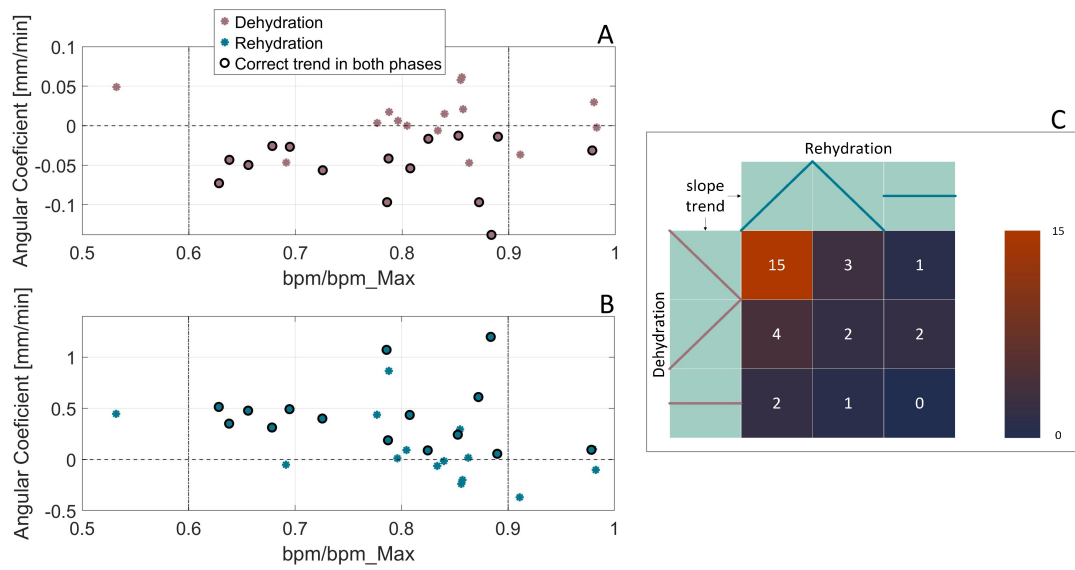


**Figure 5.6:** *Angular Coefficient (AC) distribution comparison whith %bpm in dehydration (A) and rehydration (B); Confusion Matrix of different slope trend (C).*

**Table 5.9:** *Characteristics of the angular coefficient distributions in the two phases.*

| Phase | mean | std | variation [%] |
|---|---|---|---|
| Dehydration | -0.022 | 0.046 | 2.1 |
| Rehydration | 0.26 | 0.37 | 1.4 |

### 5.3.3 Rehydration phase

In Figure 5.7, the rehydration phase is represented, considering the variation between mean, maximum, and minimum diameter values in baseline and the measurements taken 2, 4 and 6 minuteas after the rehydration. It can be observed that the return to baseline value (yellow point) occurs at different times depending on whether the mean, maximum, or minimum diameter is considered. It was calculate thanks to 4.8 obtaining:

- $t_{d\_mean} = 6.7$min;

- $t_{d\_max} = 4.7$min;

- $t_{d\_min} = 2.5$min.
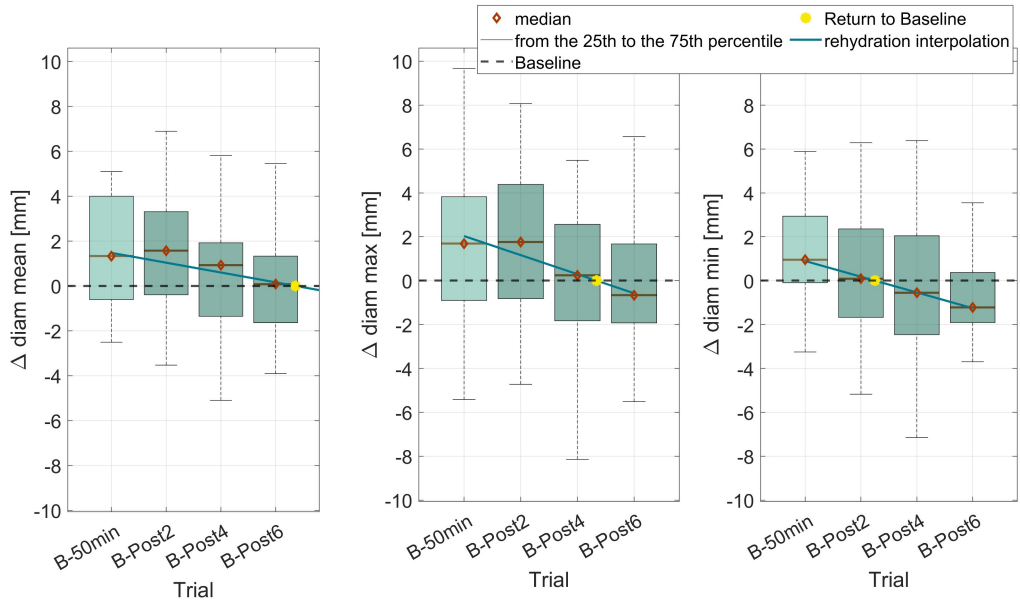


**Figure 5.7:** *Rehydration phase expressed as the difference between the baseline diameter value and measurements taken every 2 minutes after rehydration. The yellow dot indicates the time required to return to the initial diameter of the inferior vena cava.*

# 5.4   Characteristics of the k-NN model

To evaluate the degree of correlation among the various variables under analysis (Table 4.1), a correlation matrix was created, as shown in the Figure 5.9. This matrix highlights that certain variables are highly correlated with others. For instance, the standard deviation of the diameter shows a strong correlation with the caval index values. Consequently, such variables can be excluded without compromising the overall level of information. The correlation between the variables of the 30 subjects is shown in Figure 5.9. These were used for the k-NN model, and the threshold that best distinguishes between the two subject groups was selected, as explained in section 4.5. Figure 5.8 shows the accuracy levels for each trial as the threshold varies and the selected threshold. The Tables 5.10 summarize the value of k chosen, the distance considered, the threshold value, and the corresponding accuracy for each trial.
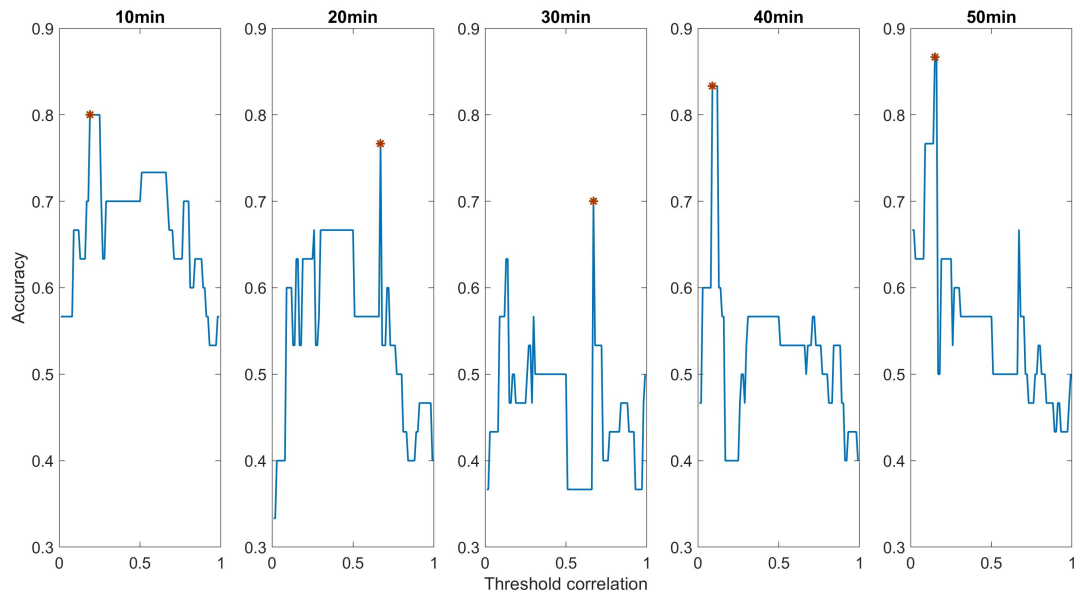


**Figure 5.8:** *Accuracy values as the chosen threshold varies for each trial.*

**Table 5.10:** *Performance and characteristics of the k-NN for each trial.*

| Trial | k | distance | threshold | accuracy | selected variables |
|-------|----|----------|-----------|----------|--------------------|
| 10 min | 61 | cosine | 0.19 | 80% | $\Delta W$, $\Delta D_{mean}$, $\Delta HR_{mean\_eco}$, $\Delta RCI_{min}$, $\Delta HR_{std\_eco}$, $\Delta CCI_{std}$ |
| 20 min | 5 | cosine | 0.67 | 76.7% | $\Delta W$, $\Delta D_{mean}$, $\Delta HR_{mean\_eco}$, $\Delta CI_{mean}$, $\Delta CCI_{mean}$, $\Delta HR_{std\_eco}$, $\Delta CI_{std}$ |
| 30 min | 1 | euclidean | 0.67 | 70% | $\Delta W$, $\Delta D_{mean}$, $\Delta HR_{mean\_eco}$, $\Delta CI_{mean}$, $\Delta CCI_{mean}$, $\Delta HR_{std\_eco}$, $\Delta CI_{std}$ |
| 40 min | 1 | cosine | 0.09 | 83.3% | $\Delta W$, $\Delta D_{mean}$, $\Delta HR_{std\_eco}$ |
| 50 min | 1 | euclidean | 0.15 | 86.7% | $\Delta W$, $\Delta D_{mean}$, $\Delta CCI_{mean}$, $\Delta HR_{std\_eco}$ |

**Figure 5.9:** *Correlation table considering all the subject.*

## 5.5 Prediction of rehydration time through the linear model

Starting from the correlation matrix (Figure 5.10) of the variables related to the 14 subjects with increasing rehydration and increasing dehydration, th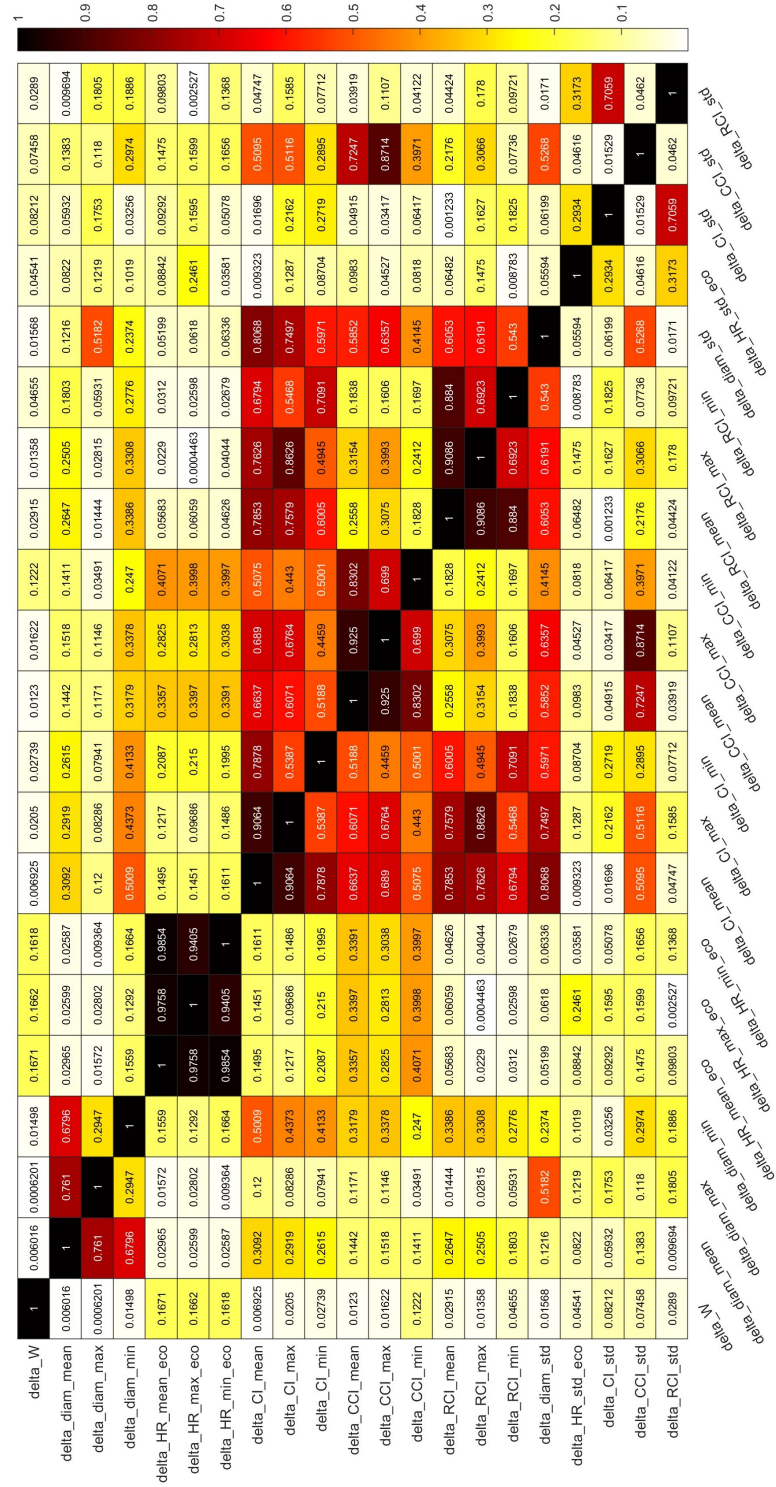e correlation threshold was selected for each trial by evaluating the performance of the models. as explained in section 4.6. The selected threshold value and the corresponding error, the chosen variables, and the linear fitting for each trial are shown in the Figures 5.11, 5.12, 5.13, 5.14, 5.15. The chosen threshold ensures good performance while preventing the model from overfitting the data. For each trial, different variables were selected, and the rehydration time, expressed in minutes, was estimated by weighting each variable with a coefficient, as shown in the formulas below. In Figure 5.16 the performance of the models for each trial is shown.

$$
\begin{aligned}
\Delta T_{10\ \text{min}} = {}& 12.42 - 4.57 \cdot \Delta W - 7.32 \cdot \Delta\overline{D} + 4.04 \cdot \Delta D_{\text{min}} + 0.06 \cdot \Delta\overline{HR}_{\text{eco}} \\
& + 5.87 \cdot \Delta\overline{CI} + 0.31 \cdot \Delta CCI_{\text{max}} - 7.92 \cdot \Delta CCI_{\text{min}} \\
& - 6.79 \cdot \Delta HR_{\text{std}} - 4 \cdot CI_{\text{std}} + 7.75 \cdot \Delta RCI_{\text{std}}
\end{aligned}
\tag{5.1}
$$

$$
\begin{aligned}
\Delta T_{20\ \text{min}} = {}& 3.77 + 19.22 \cdot \Delta W - 1.92 \cdot \Delta\overline{D} - 2.2 \cdot \Delta\overline{HR}_{\text{eco}} \\
& + 0.56 \cdot \Delta\overline{CI} - 5.95 \cdot \Delta CCI_{\text{max}} - 3.43 \cdot \Delta CCI_{\text{min}} \\
& - 1.15 \cdot \Delta HR_{\text{std}} - 4.65 \cdot \Delta CI_{\text{std}} + 6.54 \cdot \Delta RCI_{\text{std}}
\end{aligned}
\tag{5.2}
$$

$$
\Delta T_{30\ \text{min}} = 9.53 - 2.96 \cdot \Delta W - 0.3 \cdot \Delta\overline{D} - 1.39 \cdot \Delta HR_{\text{std}}
\tag{5.3}
$$

$$
\begin{aligned}
\Delta T_{40\ \text{min}} = {}& 9.94 + 1 \cdot \Delta W + 1.54 \cdot \Delta\overline{D} + 2.24 \cdot \Delta D_{\text{max}} - 1.75 \cdot \Delta D_{\text{min}} \\
& + 5.01 \cdot \Delta\overline{HR}_{\text{eco}} - 9.8 \cdot \Delta\overline{CI} + 4.62 \cdot \Delta CI_{\text{min}} + 6.72 \cdot \Delta\overline{CCI} \\
& - 4.37 \cdot \Delta CCI_{\text{max}} - 1.68 \cdot \Delta HR_{\text{std}} - 0.99 \cdot CI_{\text{std}} + 2.02 \cdot \Delta RCI_{\text{std}}
\end{aligned}
\tag{5.4}
$$

$$
\begin{aligned}
\Delta T_{50\ \text{min}} = {}& 2.43 - 7.09 \cdot \Delta W - 5.06 \cdot \Delta\overline{D} + 10.1 \cdot \Delta D_{\text{max}} - 5.92 \cdot \Delta D_{\text{min}} \\
& - 0.18 \cdot \Delta\overline{HR}_{\text{eco}} - 2.97 \cdot \Delta\overline{CI} - 5.2 \cdot \Delta\overline{CCI} + 1.16 \cdot \Delta CCI_{\text{max}} \\
& + 1.17 \cdot \Delta HR_{\text{std}} - 3.82 \cdot CI_{\text{std}} + 2.04 \cdot \Delta RCI_{\text{std}}
\end{aligned}
\tag{5.5}
$$
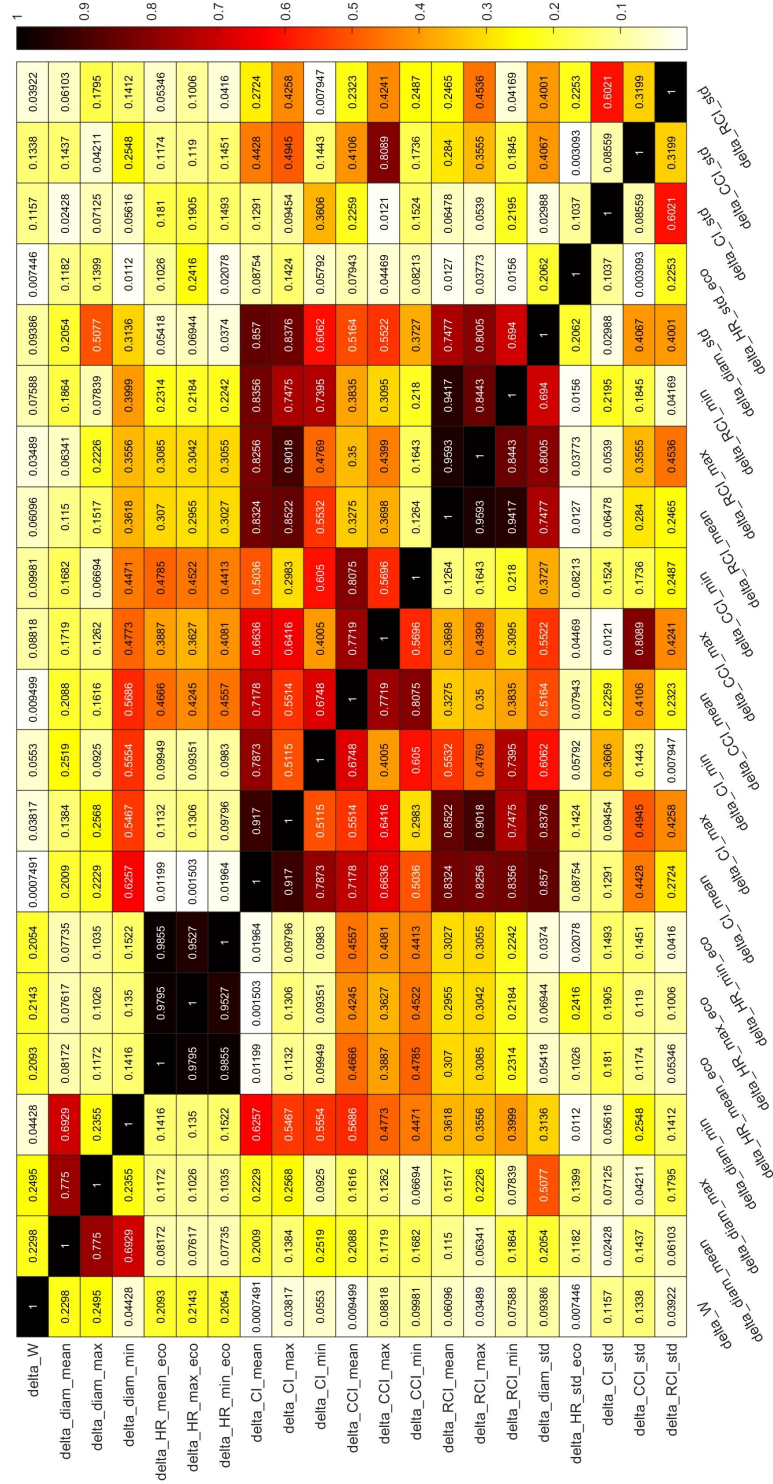
**Figure 5.10:** *Correlation table considering the 14 subject with correct trend.*
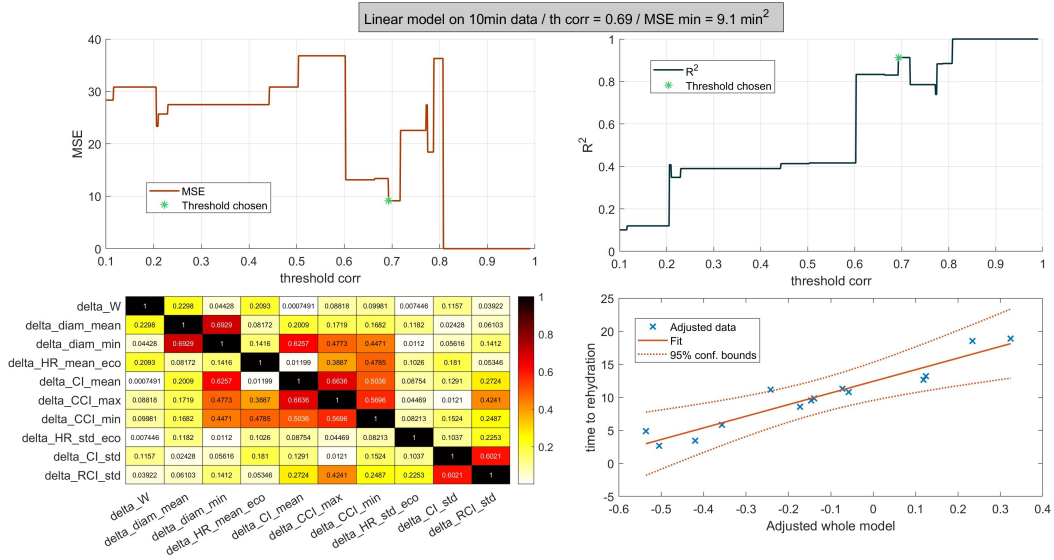
**Figure 5.11:** *Errors as the threshold changes, chosen threshold, selected variables, and linear fitting for the 10-minute test.*
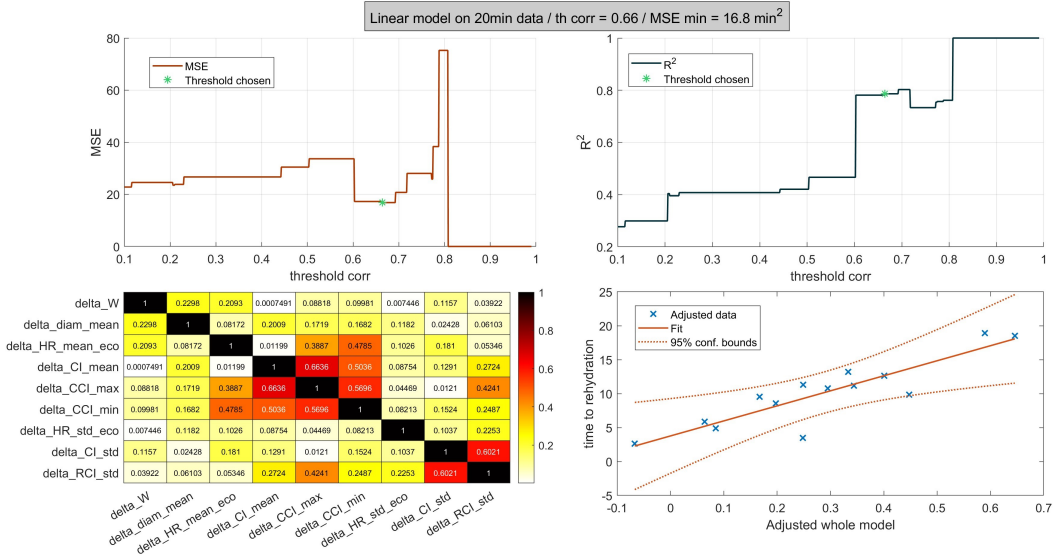


**Figure 5.12:** *Errors as the threshold changes, chosen threshold, selected variables, and linear fitting for the 20-minute test.*
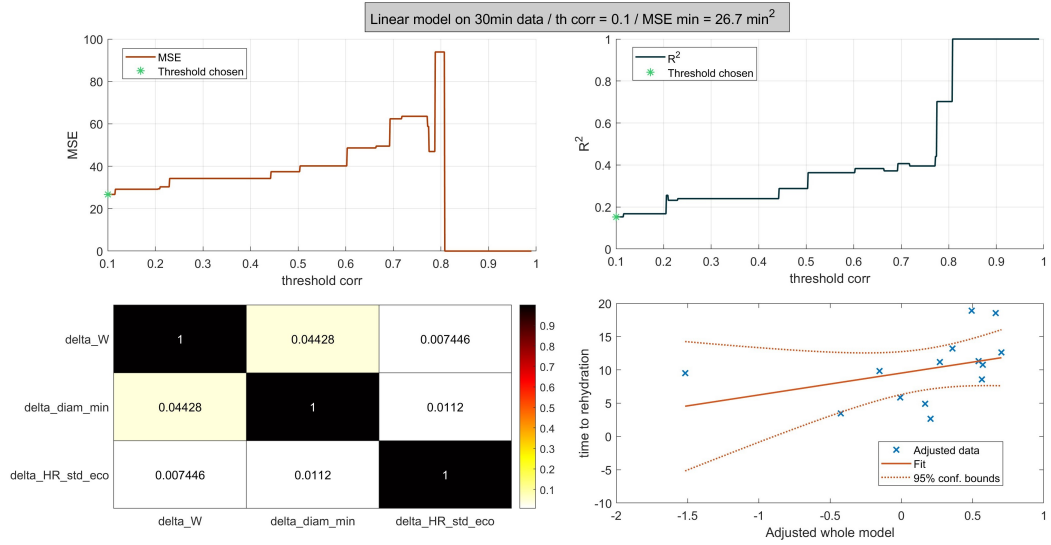
**Figure 5.13:** *Errors as the threshold changes, chosen threshold, selected variables, and linear fitting for the 30-minute test.*
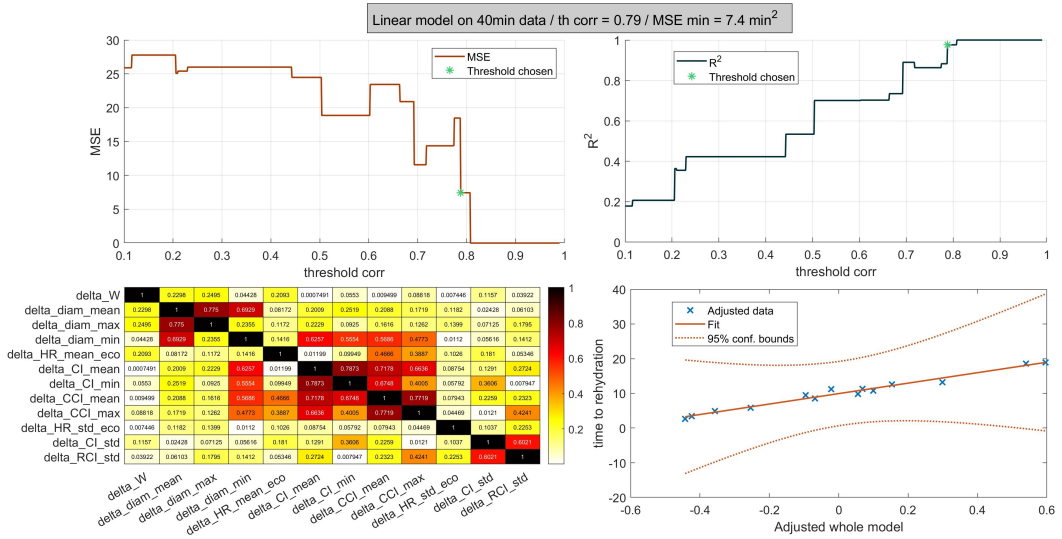


**Figure 5.14:** *Errors as the threshold changes, chosen threshold, selected variables, and linear fitting for the 40-minute testa.*
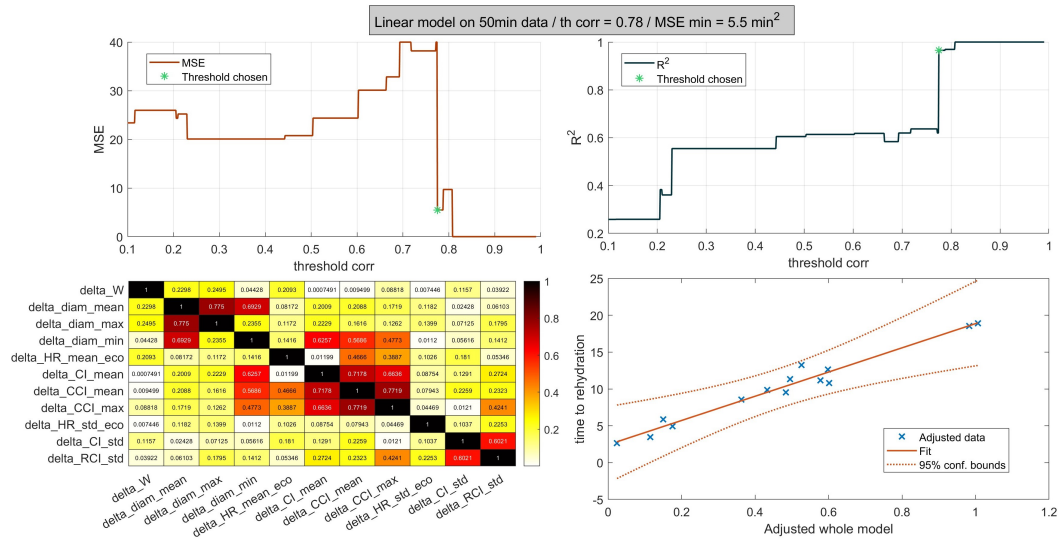
**Figure 5.15:** *Errors as the threshold changes, chosen threshold, selected variables, and linear fitting for the 50-minute test.*
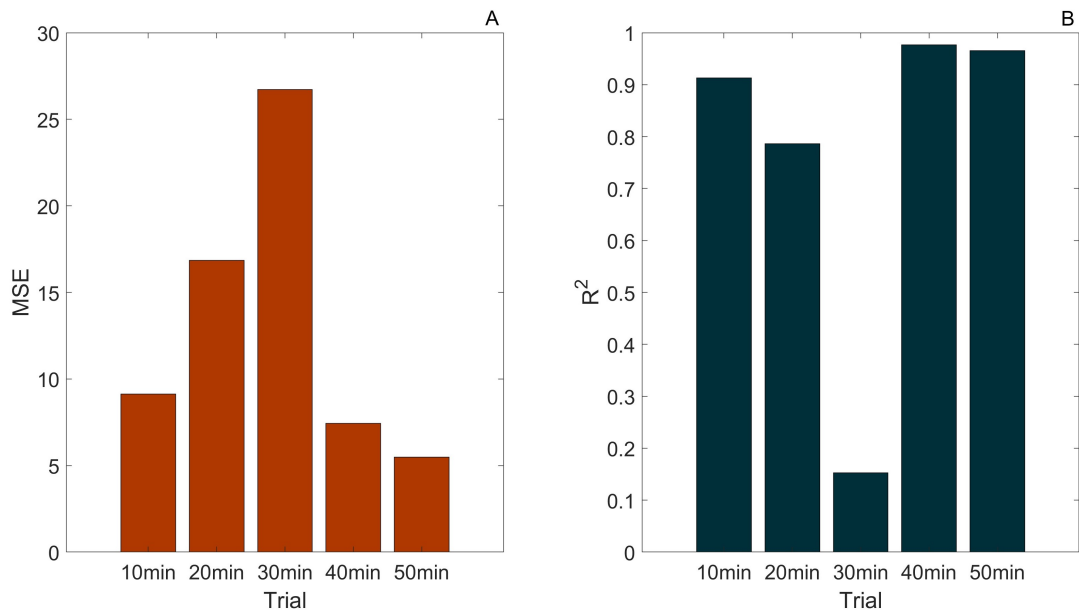


**Figure 5.16:** *Performance in term of MSE and $R^2$ of the model for each trials.*

# Chapter 6

# Discussion of the results obtained

## 6.1 Repetibility and variability of the measurements

The high degree of repeatability exhibited by the measurements serves to validate the stability of the measurements, thereby indicating that the operator, with the assistance of the software, has obtained results that are consistently reliable. The values found in this study are comparable to those reported in the literature [37], [38], where expert sonographers achieved ICC values > 0.9. This is due both to the skill of the person who performed the ultrasounds and to the software used. In fact, the software provides a diameter value for each individual frame of the ultrasound video; these values are then averaged to obtain an overall value for the entire video. This approach makes it possible to reduce the influence of any measurement errors, ensuring greater precision in the final data.

## 6.2 Evaluation of significant differences

The evaluation of significant differences revealed that during the 50 minutes of light physical activity (dehydration phase), the mean and maximum diameters of the IVC underwent a significant reduction. This is due to the fact that the vein empties as a result of fluid loss induced by sweat loss during physical activity. However, the statistically significant effect only appears between baseline values and those measured after the fifth walking repetition, suggesting that dehydration is not yet sufficiently pronounced in the intermediate steps to cause an appreciable and consistent change in vein diameter. It is possible that during the initial stages,

the body activates compensatory mechanisms to maintain adequate venous return. In particular the water is absorbed by the small intestine and enters the circulation through the capillaries, as esplained in section 1.3.3.

During the rehydration phase, a significant difference in diameter values is observed at 6 minutes post fluid replenishment. After rehydration, the body quickly redirects fluids to the vascular compartment, allowing the IVC to refill and expand, approaching baseline values. It is possible that in the first few minutes following fluid replenishment, the circulatory system is still redistributing fluids among the different compartments (intracellular, extracellular, and vascular), which is why the recovery of the IVC diameter is not immediate. Only after several minutes, once the fluid balance across the various compartments has equilibrated, does the effect of rehydration clearly manifest in an increase in venous diameter, resulting in a statistically significant difference. The minimum diameter values show a statistically significant difference only during the rehydration phase, while the caval index never shows a statistically significant difference. The maximum diameter returned by the software is lower than the value found in the literature; this may be due to a systematic measurement error or inadequate hydration of the subjects in their daily lives.

## 6.3 Analysis of trends

### 6.3.1 Interpretation of overall trends

The progressive decrease in mean diameter during the dehydration phase, followed by a subsequent increase during rehydration, aligns with expected physiological responses. The angular coefficients for each phase reveal the rate of change in diameter over time. This contrast underscores the body's capacity to recover from a state of fluid deficit when rehydration is initiated. The stability in the mean caval index (CI) during dehydration, followed by a slight decrease during rehydration, suggests that while the IVC diameter shows marked change, the CI is less susceptible to fluctuations within short-term hydration alterations. This difference may reflect the CI's role as a compensatory measure, modulating in response to prolonged or significant fluid changes rather than minor variations or the effect is not appreciable due to a high heart rate caused by physical activity. The rate of rehydration is approximately ten times greater than that of dehydration. This phenomenon may be attributed to the body's ability to absorb water at a faster rate than it loses it.

### 6.3.2   Variability subject-by-subject in angular coefficients

Analyzing individual subjects' angular coefficients, the data demonstrated normal distributions for both phases and a significant difference between dehydration and rehydration values. By comparing the standard deviation of the slope coefficients for each of the two phases and relating them to the mean, it can be observed that the percentage variations are comparable. The slope coefficients for rehydration cover a wider range compared to those for dehydration; however, rehydration exhibits a smaller variation due to its significantly higher mean value relative to that of dehydration. These differences likely stem from factors such as baseline hydration status, physical conditioning, and cardiovascular efficiency, which may impact how quickly the venous system adapts to rehydration. The percentage of heart rate, in this study, is an indicator of the fatigue experienced by the subjects, as the task required was fixed for each individual. This is highlighted in the Figure 5.6, where the only subject below the aerobic threshold is a competitive athlete engaged in an aerobic sport, while all four subjects above the anaerobic threshold do not participate in any sport. Comparing the angular coefficient values of the subjects with the percentage of heart rate, a greater dispersion of values is observed near the anaerobic threshold, both during the dehydration phase and the rehydration phase. This may be due to the fact that at low levels of fatigue, the effect of sweating is more pronounced than the confounding effects related to fatigue (such as venous return). Observing the confusion matrix, it is noted that only 15 subjects out of 30 follow the trend expected from the literature, while the other 15 present at least one phase that does not conform to the correct trend or has a slope coefficient too close to zero.

### 6.3.3   Rehydration times

The rehydration phase analyzed in the results shows a progressive reduction in the difference in inferior vena cava diameter compared to the baseline value, with return times varying depending on the measurement considered (mean, maximum, or minimum). The calculated times indicate a faster return for the minimum diameter, suggesting that rehydration initially affects the minimum diameter size, followed later by normalization of the other measurements. This result could reflect the body's ability to quickly compensate for reduced circulatory volume, initially impacting the minimum diameter of the inferior vena cava before stabilizing.

## 6.4   Division of subjects using k-NN model

As shown in Table 5.10, the best performance is achieved with the data extracted at the end of the 50-minute trial, where the effects of dehydration are likely more

pronounced. However, the data collected at 10 minutes also demonstrate significant accuracy, reaching 80%.

Moreover, the number of neighbors $k$ used for classification decreases progressively as the trials proceed: this behavior suggests that the two classes gradually move farther apart, making it sufficient to analyze only one neighbor for effective classification. Regarding the threshold value used in the reduction of correlated variables, it is observed that for the models based on the data at 10, 40, and 50 minutes, a low threshold is sufficient, leading to the selection of a smaller number of features. Conversely, for the models at 20 and 30 minutes, a higher threshold is employed, resulting in an increased number of selected variables. Nonetheless, these latter configurations do not achieve the performance of the other models. This could be attributed to a confounding effect related to the type of physical activity, which likely arises a twenty minutes after the start.

## 6.5 Predictive model for rehydration time

In order to analyze only the subjects with a positive rehydration time, a subset of the dataset was evaluated, requiring the creation of a new correlation matrix. This matrix showed correlation values similar to those obtained with the entire dataset. The most noticeable difference is observed in the correlation between $\Delta W$ and the data related to the IVC diameter. In the reduced dataset, these correlations are higher, likely due to the inclusion of subjects exhibiting similar behavior. The linear model created for each trial shows a minimum MSE value for a specific correlation threshold, except for the 30-minute model. In this case, as the threshold increases, the error also increases. This indicates that all the variables introduce noise into the model.

## 6.6 Performance estimation considering different variables after 10 minutes

The performance estimation considering different variables starting from those that achieved the highest level of accuracy after 10 minutes (Table 5.10) allows us to determine whether it is possible to distinguish between subjects after just a few minutes of activity and, consequently, predict the behavior of subjects with a decreasing dehydration trend and increasing rehydration. Moreover, using only ultrasound variables reduces the required measurement tools to just the ultrasound device, eliminating the need for a scale and a heart rate monitor, which may not always be compatible with certain types of sports. Additionally, we tested the inclusion of body weight and heart rate, one at a time, alongside the ultrasound variables. For each new set of variables, grid search was repeated, leading to

different values of *k* and distance metrics. The accuracy values were then calculated and presented in Table 6.1.

**Table 6.1:** *Characteristics of k-NN with the new datasets and accuracy level in distinguishing between subjects with correct and incorrect trends.*

| Dataset | k | distance | accuracy |
|---|---|---|---|
| all variables selected for highest perfomance | 61 | cosine | 80% |
| only eco variables | 19 | euclidean | 63.33% |
| eco variables with HR | 13 | cosine | 73.33% |
| eco variables with weight | 15 | euclidean | 66.67% |

Subsequently, the linear fit at 10 minutes was evaluated considering the 4 datasets, and the MSE values were obtained and are reported in Figure 6.1. It is observed that the best performance is achieved by considering only the ultrasound variables and those related to heart rate. This is likely due to the fact that the weight variable introduces noise, while the heart rate allows for better prediction.
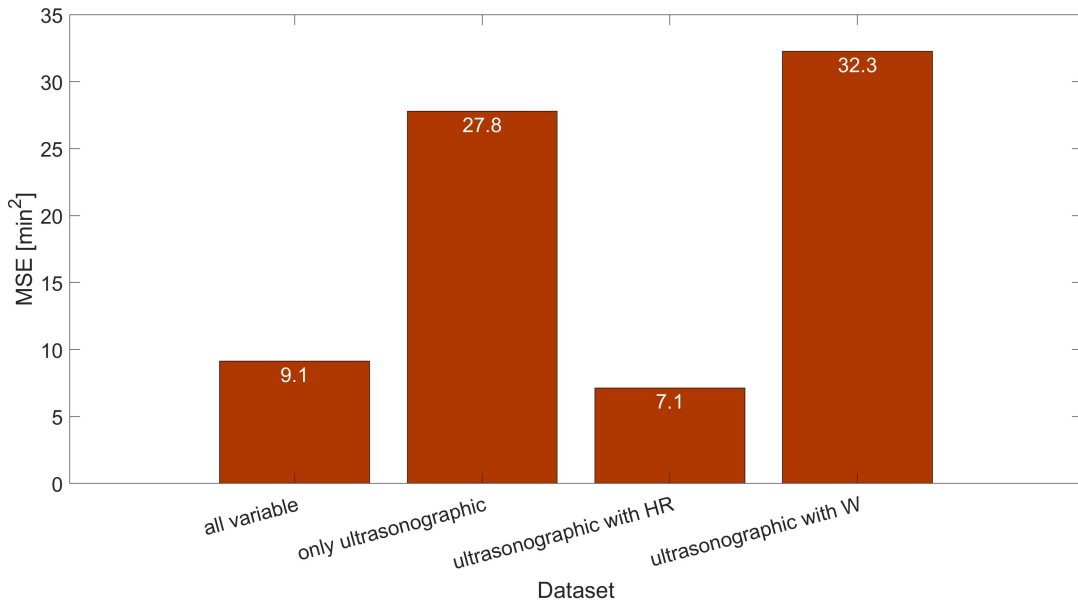


**Figure 6.1:** *MSE of the linear model after 10 minutes using different dataset.*

# Chapter 7

# Conclusions and Future Developments

## 7.1 Conclusions

This study originated from the need to overcome the limitations of traditional methods for determining hydration status, which are often invasive, time-consuming, and challenging to apply in dynamic contexts such as during athletic performance. By conducting a comprehensive investigation into the processes of dehydration and rehydration in the human body, we developed a protocol based on ultrasound imaging of the inferior vena cava. The aim was to explore whether parameters derived from this imaging modality could be correlated with the hydration status of individuals.

The analysis focused on evaluating trends in vena cava diameters and the Collapsibility Index (CI) over time. Approximately half of the sample exhibited behavior consistent with findings reported in the literature, characterized by a progressive reduction in vena cava diameter during dehydration and an expansion during rehydration. Building on these observations, we directed our attention to the rehydration phase, specifically investigating the time required for the vena cava to return to baseline conditions.

To further analyze this phenomenon, we developed a linear model that correlated rehydration times with individual dehydration dynamics. The model yielded promising results, particularly for the first, fourth, and fifth repetitions of the walking protocol. Additionally, we applied the K-Nearest Neighbors (KNN) algorithm to assess whether subjects could be divided into two groups, those whose behavior aligned with the literature and those who deviated, based on specific variables. Interestingly, as the number of repetitions increased, the KNN model required fewer neighbors to achieve an accurate classification, suggesting that with the progression

of physical activity, the two groups became increasingly distinct. The classification achieved good accuracy, reinforcing the potential of this approach.

These findings contribute to a deeper understanding of how the inferior vena cava behaves during dehydration and rehydration phases, shedding light on individual variability and its implications. Moreover, they represent a significant step forward in the development of non-invasive tools for dynamically monitoring hydration status, offering potential applications in both athletic and clinical settings.

## 7.2 Limits of the study

The first limitation of the study is related to the accuracy of the measurements, as they were performed by a non-specialized operator without proper training, using a portable probe suitable for a pilot study. It could be interesting to include a 4-electrode bioimpedance scale to measure body composition and water percentage of the sample, in order to have additional parameters with which to classify the subjects. Furthermore, to conduct this study accurately and with statistical validity, it would be advisable to increase the number of participants.

Regarding the protocol, modifications could be made to take into account the level of athleticism of the subjects: in the study in question, the task required was fixed for all subjects, regardless of their training level, which meant that highly trained individuals exerted themselves much less compared to those who were less trained. For example, the incline or speed of the treadmill could be adjusted based on the heart rate achieved. This could be done in real time by evaluating the data collected from the heart rate monitor.

Another option could be to use a stationary bike and ask the subject to keep their heart rate at a certain level so that it stays within the aerobic threshold: this is calculated using Cooper's formula (1.4) multiplied by 0.6 and knowing the subject's age. The collected data indeed show that there were a greater number of confounding effects for subjects who reached a high heart rate (Figure 5.6). Setting the heart rate percentage between 60% and 70% would ensure homogeneity among subjects and a limited number of confounding effect. Observing the Figure 7.1, it can be noted that not all subjects were in the same conditions across the various trials. For example, in the first trial, 2 subjects were below the aerobic threshold, 24 were above the aerobic threshold but below the anaerobic threshold, and 4 were above the anaerobic threshold. Furthermore, the protocol could be expanded to include a measure of body temperature, as it is strongly correlated with sweating, and a measure of room temperature to account for the environmental conditions in which the test was conducted. To observe a statistically significant difference in at least two distributions related to the dehydration phase, it is recommended to repeat the walk 6 times instead of 5. Additionally, to observe the complete return

to baseline of the mean diameter (Figure 5.7), it is necessary to take a measurement 8 minutes after rehydration.

Regarding the ultrasound measurements, it is important not to perform them in a supine position, as the transition from an upright to a lying position causes body fluids to redistribute, which alters the measurement of the diameter of the inferior vena cava that is the biggest vein of the body.

To selectively study the effects of sweating while minimizing confounding effects, it would be optimal to induce sweating in the subjects without having them engage in physical activity. This would allow for a clearer isolation of the effects of sweating, but would make it inapplicable during physical activity.

It would be interesting to consider standard methods for determining dehydration status and correlate them with parameters of the inferior vena cava, such as diameter and caval index. For instance, it could be analyze urine color as a simple indicator of hydration status and compare it with the measurements of the inferior vena cava.
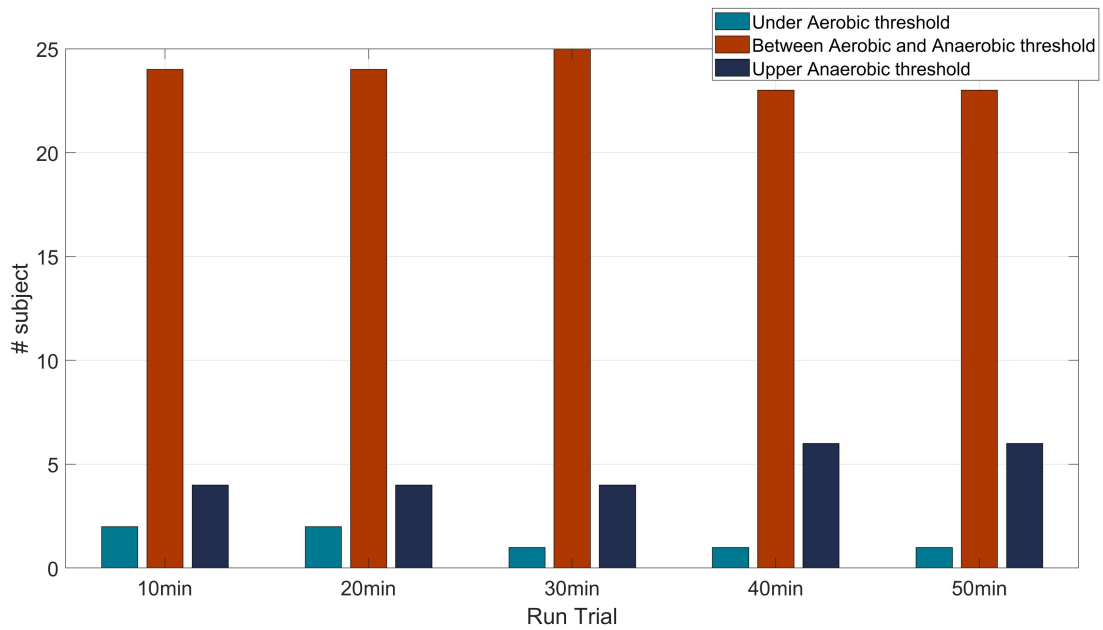


**Figure 7.1:** *Subjects' condition in the trials.*

# Bibliography

[1]  Cindy L. Stanfield. *Principles of Human Physiology*. Pearson, 2018 (cit. on pp. 1, 3, 4, 6, 8–12, 14, 15, 17, 21, 24, 26).

[2]  M. Knaflitz G.L. Cerone M. Gazzoni. *Strumentazione Biomedica*. Levrotto & Bella, 2022 (cit. on pp. 4, 5).

[3]  Luca Mesin et al. «Assessment of Phasic Changes of Vascular Size by Automated Edge Tracking-State of the Art and Clinical Perspectives». In: *Frontiers in Cardiovascular Medicine* 8 (Jan. 2022), p. 775635. DOI: `10.3389/fcvm.2021.775635` (cit. on pp. 8, 19, 35).

[4]  G. Gullace and M. T. Savoia. «Echocardiographic assessment of the inferior vena cava wall motion for studies of right heart dynamics and function». In: *Clinical Cardiology* 7.7 (July 1984), pp. 393–404. DOI: `10.1002/clc.4960070704` (cit. on p. 10).

[5]  Samuel M. Fox and John P. Naughton. «Physical activity and the prevention of coronary heart disease». In: *Preventive Medicine* 1.1 (1972), pp. 92–120. ISSN: 0091-7435. DOI: `https://doi.org/10.1016/0091-7435(72)90079-5`. URL: `https://www.sciencedirect.com/science/article/pii/0091743572900795` (cit. on p. 10).

[6]  Nicholas A. Jamnick, Robert W. Pettitt, Cesare Granata, David B. Pyne, and David J. Bishop. «An Examination and Critique of Current Methods to Determine Exercise Intensity». In: *Sports Medicine* 50 (2020), pp. 1729–1756. DOI: `10.1007/s40279-020-01322-8` (cit. on p. 10).

[7]  Ben R. Londeree and Stephen A. Ames. «Trend analysis of the % VO2 max-HR regression.» In: *Medicine and science in sports* 8 2 (1976), pp. 123–5. URL: `https://api.semanticscholar.org/CorpusID:8552412` (cit. on p. 11).

[8]  J. P. Desai and F. Moustarah. «Pulmonary Compliance». In: *StatPearls* (Jan. 2024). [Internet]. URL: `https://www.ncbi.nlm.nih.gov/books/NBK539757/` (cit. on p. 15).

[9]  Benjamin J Kimura, Raynier Dalugdugan, Gregory W 3rd Gilcrease, John N Phan, Brett K Showalter, and Theodore Wolfson. «The effect of breathing manner on inferior vena caval diameter». In: *European Journal of Echocardiography* 12.2 (Feb. 2011), pp. 120–123. DOI: 10.1093/ejechocard/jeq157. URL: https://doi.org/10.1093/ejechocard/jeq157 (cit. on p. 19).

[10]  Anna Folino, Marco Benzo, Paolo Pasquero, Andrea Laguzzi, Luca Mesin, Alessandro Messere, Massimo Porta, and Silvestro Roatta. «Vena Cava Responsiveness to Controlled Isovolumetric Respiratory Efforts». In: *Journal of Ultrasound in Medicine* 36.10 (2017), pp. 2113–2123. DOI: https://doi.org/10.1002/jum.14235. eprint: https://onlinelibrary.wiley.com/doi/pdf/10.1002/jum.14235. URL: https://onlinelibrary.wiley.com/doi/abs/10.1002/jum.14235 (cit. on p. 19).

[11]  Bojan Knapl. «Hydration and Physical Activity». In: *Research & Investigations in Sports Medicine* 7 (Apr. 2021) (cit. on p. 20).

[12]  Francesco Visioli Andrea Poli. «Idratazione e salute». In: (2009) (cit. on p. 20).

[13]  Samuel Cheuvront and Michael Sawka. «Hydration Assessment of Athletes». In: *Sports Sci Exchange Number 2* 18 (Jan. 2005), p. 97 (cit. on pp. 20, 33).

[14]  Jordi Salas-Salvado and et al. «Importancia del consumo de agua en la salud y la prevención de la enfermedad: situación actual». In: *Nutr. Hosp.* 37.5 (2020). Epub 04-Ene-2021, ISSN 1699-5198, pp. 1072–1086. DOI: https://dx.doi.org/10.20960/nh.03160. URL: http://scielo.isciii.es/scielo.php?script=sci_arttext&pid=S0212-16112020000700026&lng=es&nrm=iso (visited on 10/17/2024) (cit. on p. 20).

[15]  Maurizio Schiavon, Pierantonio Michieli, Daniele Bordin, and Walter Pasini. «L'Idratazione nello sportivo». In: *Biblioteca dello sport di Padova* (2008) (cit. on pp. 21–23).

[16]  P.O. Astrand, K. Rodhal, and A. Resiano. *Fisiologia di Astrand e Rodhal*. Edi. Ermes, 1984. ISBN: 9788870510140. URL: https://books.google.it/books?id=t9pJAAAACAAJ (cit. on p. 22).

[17]  Lindsay B. Baker. «Physiology of sweat gland function: The roles of sweating and sweat composition in human health». In: *Temperature* 6.3 (2019). PMID: 31608304, pp. 211–259. DOI: 10.1080/23328940.2019.1632145. eprint: https://doi.org/10.1080/23328940.2019.1632145. URL: https://doi.org/10.1080/23328940.2019.1632145 (cit. on p. 24).

[18]  Thomas G.Nyland John S. Mattoon. *Principi fondamentali di ecografia diagnostica* (cit. on pp. 27, 31, 41).

[19]  G.Coppini G.Valli. *Bioimmagini*. Pàtron, 2002 (cit. on pp. 27–30).

[20]   Daniel J Wallace, Matthew Allison, and Michael B Stone. «Inferior vena cava percentage collapse during respiration is affected by the sampling location: an ultrasound study in healthy volunteers». In: *Academic Emergency Medicine* 17.1 (Jan. 2010), pp. 96–99. DOI: `10.1111/j.1553-2712.2009.00627.x` (cit. on p. 32).

[21]   Ann C. Grandjean and Nicole R. Grandjean. «Dehydration and Cognitive Performance». In: *Journal of the American College of Nutrition* 26.sup5 (2007). PMID: 17921464, 549S–554S. DOI: `10.1080/07315724.2007.10719657`. eprint: 57. URL: `https://doi.org/10.1080/07315724.2007.10719657` (cit. on p. 33).

[22]   Copping JR. Gisolfi CV. «Thermal effects of prolonged treadmill exercise in the heat». In: *Medicine & Science in Sports & Exercise* (1974) (cit. on p. 33).

[23]   Montain SJ. Coyle EF. «Benefits of fluid replacement with carbohydrate during exercise». In: *Medicine & Science in Sports & Exercise* (1992) (cit. on p. 33).

[24]   B. E. Robinson and H. Weber. «Dehydration despite drinking: beyond the BUN/Creatinine ratio». In: *Journal of the American Medical Directors Association* 5.2 (Mar. 2004), S67–71. DOI: `10.1097/01.JAM.0000035860.71185.39` (cit. on p. 34).

[25]   L. E. Armstrong. «Assessing hydration status: the elusive gold standard». In: *Journal of the American College of Nutrition* 26.5 Suppl (Oct. 2007), 575S–584S. DOI: `10.1080/07315724.2007.10719661` (cit. on p. 34).

[26]   A Riccardi, B Chiarbonello, P Minuto, G Guiddo, L Corti, and R Lerza. «Identification of the hydration state in emergency patients: correlation between caval index and BUN/creatinine ratio». In: *European review for medical and pharmacological sciences* 17.13 (July 2013), pp. 1800–1803 (cit. on p. 35).

[27]   Daniele Orso, Nicola Guglielmo, Nicola Federici, Francesco Cugini, Angelo Ban, Filippo Mearelli, and Roberto Copetti. «Accuracy of the caval index and the expiratory diameter of the inferior vena cava for the diagnosis of dehydration in elderly». In: *J Ultrasound* 19.3 (2016), pp. 203–209. DOI: `10.1007/s40477-016-0200-y` (cit. on p. 35).

[28]   Ajay Dipti, Zachary Soucy, Aarti Surana, and Satish Chandra. «Role of inferior vena cava diameter in assessment of volume status: a meta-analysis». In: *The American Journal of Emergency Medicine* 30.8 (Oct. 2012), 1414–1419.e1. DOI: `10.1016/j.ajem.2011.10.017` (cit. on p. 35).

[29] Anna L. Waterbrook, Amish Shah, Elisabeth Jannicky, Uwe Stolz, Randy P. Cohen, Austin Gross, and Srikar Adhikari. «Sonographic Inferior Vena Cava Measurements to Assess Hydration Status in College Football Players During Preseason Camp». In: *Journal of Ultrasound in Medicine* 34.2 (2015), pp. 239–245. DOI: `https://doi.org/10.7863/ultra.34.2.239`. eprint: `https://onlinelibrary.wiley.com/doi/pdf/10.7863/ultra.34.2.239`. URL: `https://onlinelibrary.wiley.com/doi/abs/10.7863/ultra.34.2.239` (cit. on p. 35).

[30] E. Ragaisyte, L. Bardauskiene, E. Zelbiene, L. Darginavicius, E. Zemaityte, N. Jasinskas, and K. Stasaitis. «Evaluation of volume status in a prehospital setting by ultrasonographic measurement of inferior vena cava and aorta diameters». In: *Turkish Journal of Emergency Medicine* 18.4 (Sept. 2018), pp. 152–157. DOI: `10.1016/j.tjem.2018.07.002` (cit. on pp. 35, 39).

[31] Kristofer Hedman, Eva Nylander, Jan Henriksson, Niclas Bjarnegård, Lars Brudin, and Éva Tamás. «Echocardiographic Characterization of the Inferior Vena Cava in Trained and Untrained Females». In: *Ultrasound in Medicine & Biology* 42.12 (2016), pp. 2794–2802. ISSN: 0301-5629. DOI: `https://doi.org/10.1016/j.ultrasmedbio.2016.07.003`. URL: `https://www.sciencedirect.com/science/article/pii/S0301562916301624` (cit. on p. 35).

[32] Luca Mesin, Tommaso Giovinazzo, Stefano D'Alessandro, Silvestro Roatta, Alessandra Raviolo, Francesca Chiacchiarini, Massimo Porta, and Paolo Pasquero. «Improved Repeatability of the Estimation of Pulsatility of Inferior Vena Cava». In: *Ultrasound Med Biol* 45.10 (Oct. 2019), pp. 2830–2843. DOI: `10.1016/j.ultrasmedbio.2019.06.002`. URL: `https://doi.org/10.1016/j.ultrasmedbio.2019.06.002` (cit. on pp. 44, 46).

[33] Luca Mesin, Paola Pasquero, Silvia Albani, Marco Porta, and Silvestro Roatta. «Semi-automated tracking and continuous monitoring of inferior vena cava diameter in simulated and experimental ultrasound imaging». In: *Ultrasound in Medicine & Biology* 41.3 (2015), pp. 845–857. DOI: `10.1016/j.ultrasmedbio.2014.09.031` (cit. on p. 46).

[34] Luca Mesin, Paola Pasquero, and Silvestro Roatta. «Tracking and Monitoring Pulsatility of a Portion of Inferior Vena Cava from Ultrasound Imaging in Long Axis». In: *Ultrasound in Medicine & Biology* 45.5 (2019), pp. 1338–1343. DOI: `10.1016/j.ultrasmedbio.2018.10.024` (cit. on p. 46).

[35] Laura Ermini, Sergio Seddone, Paolo Policastro, Luca Mesin, Paola Pasquero, and Silvestro Roatta. «The Cardiac Caval Index: Improving Noninvasive Assessment of Cardiac Preload». In: *Journal of Ultrasound in Medicine* 41.9 (2022), pp. 2247–2258. DOI: `10.1002/jum.15909` (cit. on p. 46).

[36] Luca Mesin, Paolo Pasquero, and Silvestro Roatta. «Multi-directional Assessment of Respiratory and Cardiac Pulsatility of the Inferior Vena Cava From Ultrasound Imaging in Short Axis». In: *Ultrasound in Medicine & Biology* 46.12 (2020), pp. 3475–3482. ISSN: 0301-5629. DOI: `10.1016/j.ultrasmedbio.2020.08.027`. URL: `https://www.sciencedirect.com/science/article/pii/S030156292030394X` (cit. on p. 46).

[37] D. Blanca, E. C. Schwarz, T. J. Olgers, et al. «Intra-and inter-observer variability of point of care ultrasound measurements to evaluate hemodynamic parameters in healthy volunteers». In: *Ultrasound J* 15.22 (2023). DOI: `10.1186/s13089-023-00322-9`. URL: `https://doi.org/10.1186/s13089-023-00322-9` (cit. on pp. 48, 70).

[38] Sara Bosio, Marta Barba, Annalisa Vigna, Alice Cola, Desirèe De Vicari, Clarissa Costa, Silvia Volontè, and Matteo Frigerio. «A Novel Method for the Measurement of the Vaginal Wall Thickness by Transvaginal Ultrasound: A Study of Inter- and Intra-Observer Reliability». In: *Medicina* 60.3 (2024). ISSN: 1648-9144. DOI: `10.3390/medicina60030370`. URL: `https://www.mdpi.com/1648-9144/60/3/370` (cit. on pp. 48, 70).

# Acknowledgements